UNIVERSITÀ CA' FOSCARI VENEZIA

CORSO DI LAUREA MAGISTRALE IN

SCIENZE AMBIENTALI

Capitale naturale e servizi ecosistemici

TESI DI LAUREA

Development and calibration of a hydrological model for flood prediction in the Cordevole stream

Relatore: Prof. Enrico Bertuzzo

Correlatore: Dott. Francesco Presotto

Laureando: Giacomo Masarin

Matricola: 908903

Anno Accademico 2025/2026

Abstract

This thesis aims to develop and calibrate a hydrological model for flood prediction in the Cordevole stream, a tributary of the Piave river. The study is based on the coupling of two distinct numerical models. Initially, the rainfall-runoff modeling was developed in the MATLAB environment using the semi-distributed hydrological model RHYME. A key aspect of this phase involved characterizing the hydrological balance through the accurate estimation of the crop coefficient (Kc), which was calculated based on the specific land use classes of the basin to evaluate evapotranspiration and net rainfall. The hydrographs generated by RHYME were then used as upstream boundary conditions for the one-dimensional (1D) hydraulic modeling of the river channel, performed using the HEC-RAS software. The simulations, conducted under unsteady flow conditions, required precise geometric extraction of cross-sections from DTMs and careful management of numerical instabilities related to the steep mountain slopes. In conclusion, integrating the hydrological model with the hydraulic routing model allowed for an accurate reconstruction of water depths and wave propagation dynamics, providing a solid methodological approach for the integrated modeling of complex basins.

Declaration on the Use of Artificial Intelligence

The undersigned Giacomo Masarin, student ID 908903, enrolled at Ca' Foscari University of Venice in the Master's Degree in Environmental Sciences, author of the thesis *Development and calibration of a hydrological model for flood prediction in the Cordevole stream*, supervisor Prof. Enrico Bertuzzo, aware of the sanctions provided for by art. 76 of the Consolidated Text, D.P.R. 28/12/2000 n. 445, under his personal responsibility pursuant to artt. 46 and 47 of D.P.R 28/12/2000 n. 445,

DECLARES

to have made use of generative artificial intelligence tools to support certain parts of this thesis, specifically:

- **Claude (Anthropic), model Claude Sonnet 4.6**, used for:
  - translation and reformulation of technical concepts from Italian to English;
  - revision and linguistic optimization of texts to improve clarity, coherence, and scientific writing style;
  - support in the graphical formatting of tables and figures, including the preparation of MATLAB plotting code for the visualization of results;
  - general support during the writing process;
- **NotebookLM (Google)**, used for:
  - analysis and consultation of bibliography sources, including summarization and cross-referencing of scientific papers relevant to the thesis topics (hydrological modelling, evapotranspiration, Bayesian calibration);
- **Gemini Pro (Google)**, used for:
  - support in understanding and clarifying technical and scientific concepts encountered during the research phase;
  - assistance in explaining and formulating written descriptions of complex concepts;

Sections involved: all chapters of the thesis

Verification of accuracy: all text, code, and graphical outputs produced or reworked with the support of any of the above tools were re-read, tested, and approved by the author, who verified their correspondence with the original data and the cited bibliographic sources. The supervisor reviewed the scientific content of the thesis.

FURTHER DECLARES

that all material produced or reworked with AI support has been carefully verified and revised by the author, who assumes full responsibility for the quality, accuracy, and scientific integrity of the work.

Contents

List of Figures

List of Tables

Chapter 1

Introduction

Flood events are among the most destructive natural hazards in Alpine regions. Steep catchments and intense precipitation episodes combine to produce rapid, high-magnitude responses that challenge both prediction and management. Hydrological models are a key tool in this context: calibrated against observed discharge records, they can simulate catchment responses to rainfall, estimate peak discharges, and provide boundary conditions for hydraulic inundation models.

In the Veneto region, models developed by the Department of Civil, Environmental and Architectural Engineering (ICEA) of the University of Padova have been integrated into the Delft-FEWS operational platform, giving rise to the IMAGeOnFEWS flood forecasting system, [4]. The system couples RHYME, a semi-distributed rainfall-runoff model based on a geomorphological instantaneous unit hydrograph [12], with the two-dimensional finite-element hydrodynamic model 2DEF for flood wave propagation. It is currently operational for both the Brenta-Bacchiglione and Piave catchments.

This thesis focuses on the Cordevole stream, a right-bank tributary of the Piave draining an Alpine catchment in the Dolomites of northeastern Italy. Within the Piave operational system, Ponte Mas – the gauging station at the Cordevole outlet – is one of the calibration sections of the regional hydrological model and one of the sections for which flood alert thresholds are issued [4]. The September 1999 event, which produced one of the highest recorded discharge peaks at this station, serves as the reference flood for the hydraulic simulations carried out in this work.

The version of RHYME available at the beginning of this study had three main limitations. Reference evapotranspiration was computed through a simplified routine that did not account for spatial variability of land cover across sub-catchments: the crop coefficient was a single calibrated scalar, uniform in space and constant through the year. The numerical integration of the soil water balance used a forward Euler scheme with a fixed one-hour time step, which can produce non-physical results when saturation changes rapidly within a single step – a situation that arises frequently during high-intensity events or when the leaching function is strongly nonlinear.

The objective of this thesis is to implement and calibrate an updated version of RHYME for the Cordevole basin. The specific contributions are:

- A monthly, spatially distributed crop coefficient K_c for each sub-catchment, derived from the CORINE Land Cover dataset following [10].

- Replacement of the original ET_0 routine — itself based on a simplified form of the Penman-Monteith equation that omitted elevation-dependent corrections for atmospheric pressure and used a fixed psychrometric constant — with the full FAO-56 Penman-Monteith implementation [1].
- An adaptive sub-stepping scheme for the soil water balance, in which fluxes are resolved sequentially and the sub-step duration is refined when the saturation state changes rapidly.
- Estimation of the geomorphological routing parameters celerity of the wave propagation u and hydrodynamic dispersivity D_h from a one-dimensional HEC-RAS simulation [2] of the September 1999 event, replacing their free calibration.
- Bayesian calibration of the updated model using the DREAM algorithm [14].

Chapter 2

Study Area

2.1 The Cordevole Catchment

The Cordevole River is the primary right-bank tributary of the Piave River, draining a catchment located entirely within the Province of Belluno in the Dolomites of northeastern Italy. The stream rises near the Pordoi pass at 1919 m a.s.l. and flows southwards to join the Piave near Mel; for the purpose of this study, however, the reference outlet is the Ponte Mas gauging station (Figure 2.1), which closes a drainage area of 700.3 km^2.

The basin has a pronounced Alpine relief. Sub-catchment mean elevations, derived from DTM analysis, range from a minimum of 702.8 m to 2083.8 m a.s.l., and the highest peaks exceed 3300 m a.s.l., culminating with the Marmolada glacier at the northern boundary. The hydrographic network is correspondingly complex: the main tributaries resolved within the RHYME model discretization are the Fiorentina, Pettorina, Mis, Rova, Tegnas, Rio Andraz and Biois streams, each contributing to the runoff response at Ponte Mas through distinct sub-catchments of varying size and elevation (Figure 2.1b).

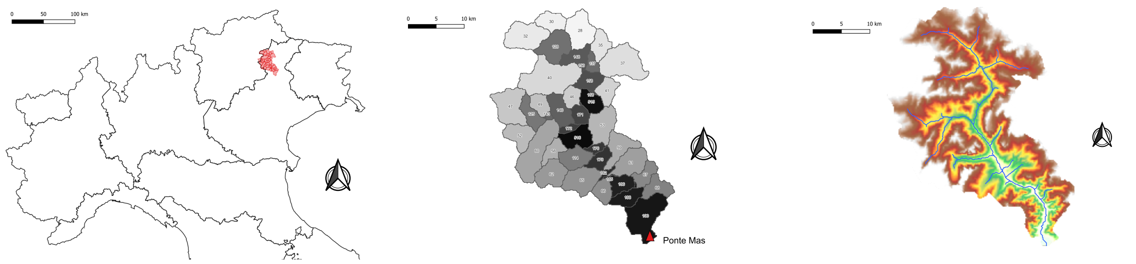

(a) Geographic location (b) Sub-catchments (c) Elevation (m a.s.l.)

Figure 2.1: Overview of the Cordevole study area. (a) Location within northeastern Italy; (b) spatial discretization into 42 semi-distributed sub-catchments for the RHYME model; (c) digital terrain model showing the steep, dissected topography of the basin.

2.2 Hydrographic Network Extraction

The sub-catchment discretization used in the RHYME model was derived from the DTM of the upper Piave–Cordevole area through standard GIS terrain analysis. The workflow follows four sequential steps: slope computation, flow direction assignment, flow accumulation, and stream network extraction with sub-catchment delineation.

Surface gradient was computed first (Figure 2.2). The slope map confirms the steep, dissected character of the basin: values locally exceed 200%, particularly along the subvertical dolomite and limestone outcrops of the upper catchment, while the valley floors show markedly gentler gradients.

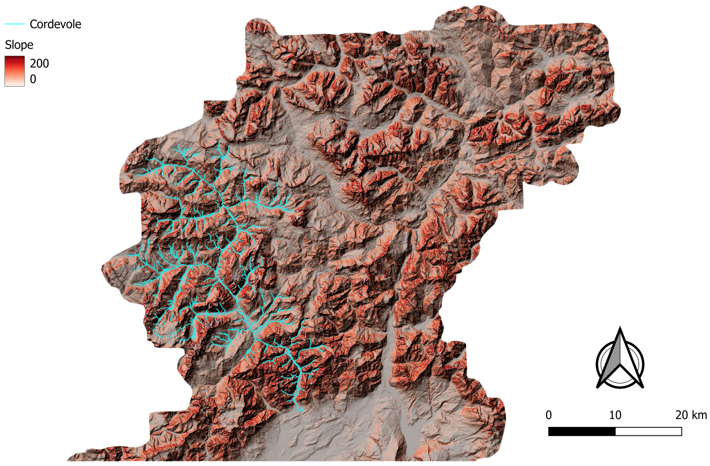

Figure 2.2: Slope map of the upper Piave–Cordevole area derived from the DTM, expressed as percentage gradient. High-slope zones (red) correspond to the subvertical dolomite limestone outcrops of the upper basin.

Flow direction was assigned to each cell using the D8 single-flow-direction algorithm, which routes runoff toward the steepest of the eight cardinal and diagonal neighbors (Figure 2.3). The resulting raster was then used to compute flow accumulation — the number of upstream cells draining through each point (Figure 2.4, shown on a $\log_{10}$ scale). Cells with high accumulation values trace the main channel of the Cordevole and its principal tributaries.

Applying an accumulation threshold to extract the stream network and defining pour points at confluences and at the basin outlet yielded the 42 sub-catchments (Figure 2.5) adopted in the RHYME discretization.

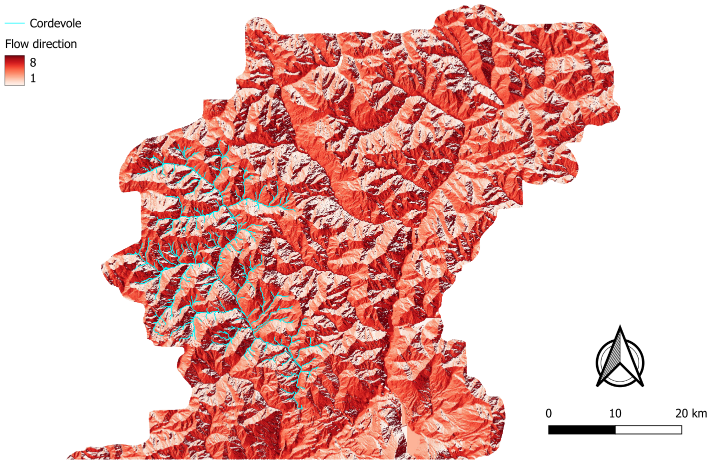

Figure 2.3: Flow direction raster computed from the DTM using D8 algorithm. Each cell is assigned one of eight possible flow directions toward its steepest-descent neighbor

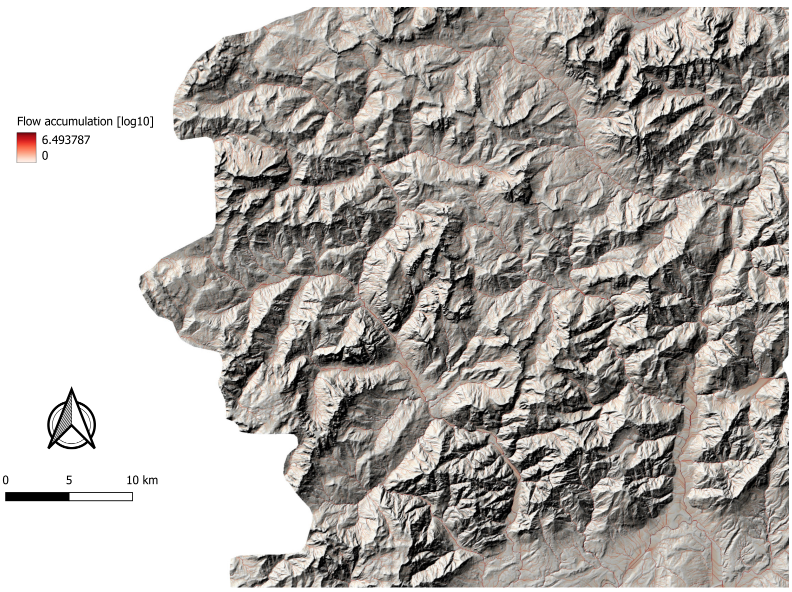

Figure 2.4: Flow accumulation raster ($\log_{10}$ scale). High-accumulation cells identify the channel network; a threshold on this field was used to extract the stream network and define sub-catchment boundaries.

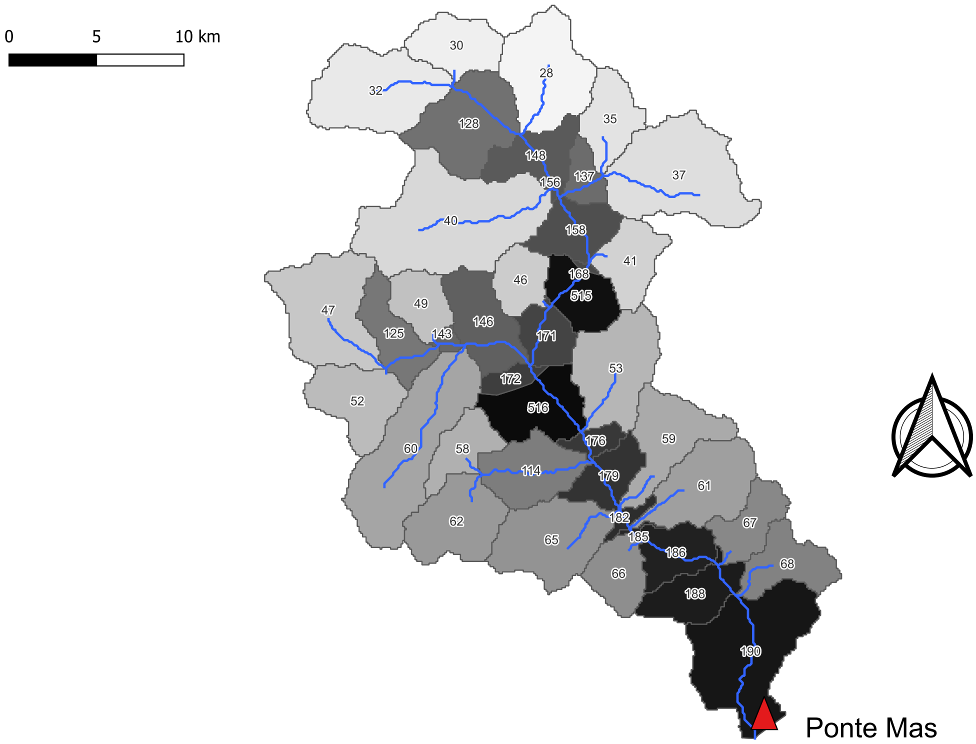

Figure 2.5: Sub-catchment delineation and extracted stream network of the Cordevole basin.

2.3 Geology and Land Cover

The geology of the basin reflects the structural complexity of the Dolomites. The upper catchment is dominated by dolomite, limestone, and volcanic rocks that form subvertical cliffs and extensive bare rock surfaces. Moving downslope, the valley flanks are underlain by more erodible sedimentary formations and quaternary deposits, making the area susceptible to diffuse mass wasting and debris flow activity [11]. This lithological contrast between the resistant high-altitude outcrops and the softer lower slopes is mirrored in the topography visible in Figure 2.2.

Land Cover follows the elevation gradient closely. According to the CORINE Land Cover (CLC) dataset [3], coniferous and mixed forests dominate the mid-elevation slopes, giving way to natural grasslands, bare rock, and sparse vegetation above the treeline. Agricultural and urban land uses together cover less than 3% of the basin, confined to the narrow valley floors around Agordo and Alleghe. The resulting land cover is spatially heterogeneous and strongly seasonal in its vegetative activity, which justifies the implementation of distributed, monthly crop coefficient K_c for evapotranspiration modelling, one of the main contributions of this work.

2.4 Climate and Hydrological Regime

Mean annual precipitation over the basin is 1352 mm, distributed unevenly across the year and strongly modulated by altitude and exposure. The flow regime at Ponte Mas is typical of Alpine environments: discharge peaks in spring, driven by snowmelt (May–June), and reaches its seasonal minimum in winter months (January–February) when most precipitation is stored as snowpack. Autumn brings a second period of elevated discharge, generated by intense rainfall events of short to medium duration that can trigger rapid, high-magnitude flood response.

The September 1999 event is the most notable example in the observation record. It produced one of the highest discharge peaks measured at Ponte Mas and it is used as the reference event for the HEC-RAS hydraulic simulations presented in Chapter 5. A further element shaping the hydrological regime is Lake Alleghe, a natural lake formed by a large landslide in 1771. Located on the main stem of the Cordevole upstream of Agordo, it acts as a small natural reservoir and attenuates flood peaks locally, though its effect is not explicitly resolved in the hydrological model.

Chapter 3

Theory and Numerical Models

This chapter describes the mathematical formulations underlying the models used in this study. The first part covers RHYME, with particular attention to evapotranspiration, snow accumulation and melt, the soil water balance, and geomorphological routing. The second part presents the one-dimensional hydraulic model implemented in HEC-RAS. The chapter closes with the Bayesian inference framework and the DREAM algorithm adopted for parameter estimation and uncertainty quantification.

3.1 The RHYME Hydrological Model

RHYME (River HYdrological Model spatially Explicit) is a semi-distributed, physically-based hydrological model for rainfall–runoff simulation at the catchment scale. The model is adapted from the SEHR-ECHO model [13], by removing the glacier component which is not relevant for the catchment under study, and it is used by the Veneto Civil Protection Authority for operational flood forecasting within the IMA-GeOnFEWS platform. The spatial domain is partitioned into sub-catchments through GIS pre-processing of a Digital Terrain Model (DTM); within each sub-catchment, forcing and state variables are treated as spatially uniform.

The model operates on two coupled process domains. At the hillslope scale, incoming precipitation — corrected for snow accumulation and melt — is partitioned into infiltration, surface runoff (generated when the soil is saturated or when precipitation exceeds the maximum infiltration capacity I_{max}), actual evapotranspiration, and deep percolation. At the network scale, the resulting water fluxes are routed along the channel network to the catchment outlet. Figure 3.1 shows the overall model structure.

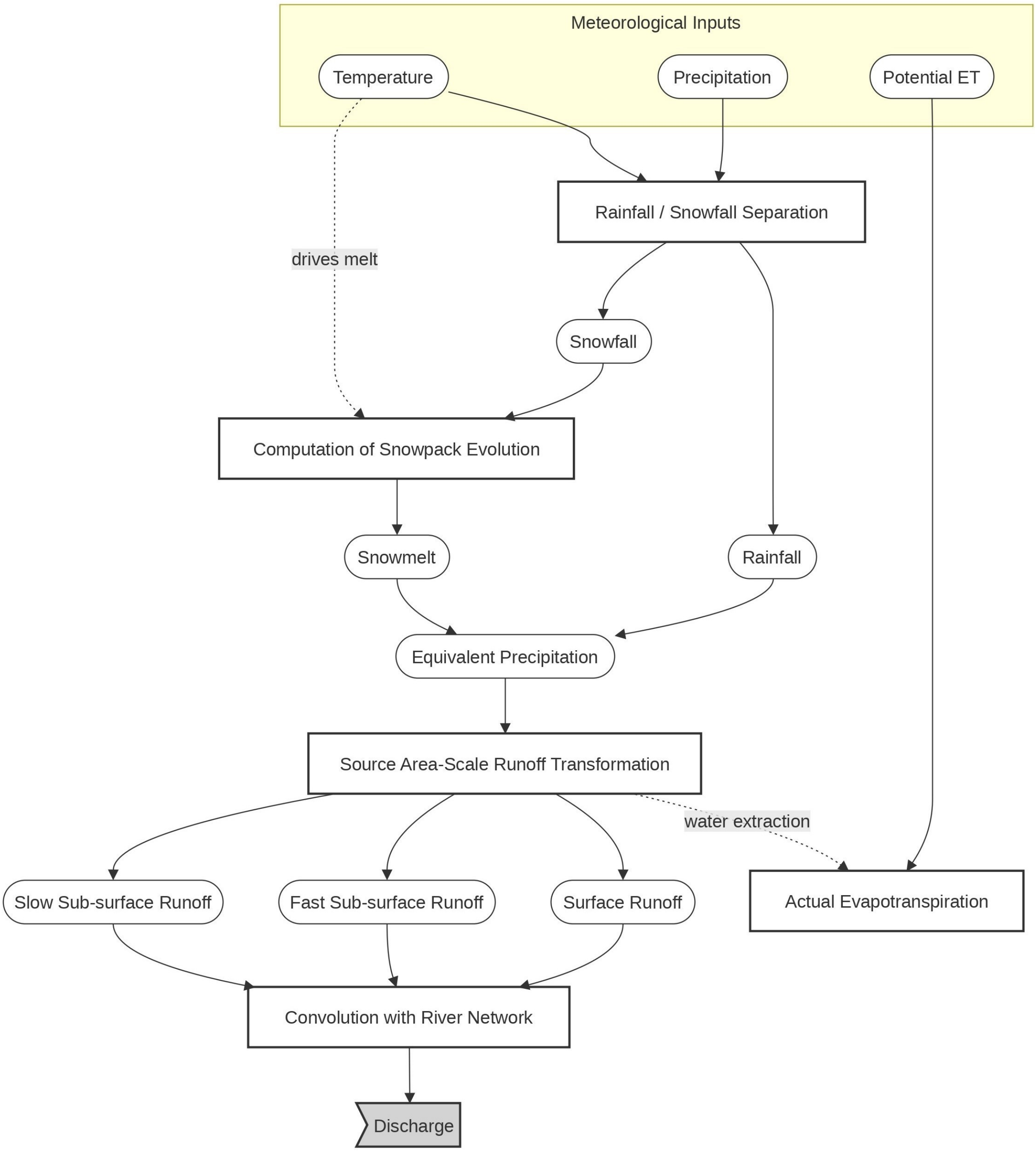

Figure 3.1: Conceptual structure of the RHYME hydrological model. Meteorological inputs are first processed through the temperature-index snow module, then partitioned across the soil moisture balance (infiltration, deep drainage, and actual evapotranspiration subject to water-stress). Hillslope fluxes are distributed across four parallel linear reservoirs and routed to the outlet via the geomorphological Instantaneous Unit Hydrograph (IUH)

3.1.1 Evapotranspiration

Evapotranspiration is a major component of the catchment water balance, particularly in forested Alpine basins where vegetative demand can account for a substantial fraction of annual precipitation. In RHYME, actual evapotranspiration ET is estimated following the crop coefficient of [1], which separates the atmospheric evaporative demand from the vegetation and soil response.

Reference evapotranspiration ET_0 quantifies the evaporative demand of the atmosphere over a standardized grass surface under non-limiting water conditions. It is computed using the FAO-56 Penman-Monteith equation [1].

$$ET_0 = \frac{0.408\,\Delta\,(R_n - G) + \gamma \frac{900}{T+273}\,u_2\,(e_s - e_a)}{\Delta + \gamma\,(1 + 0.34\,u_2)} \tag{3.1}$$

where Δ is the slope of the saturation vapor pressure curve, R_n is net radiation, G is the soil heat flux density, γ is the psychrometric constant, T is mean daily air temperature, u_2 is wind speed at 2 m height, and $e_s - e_a$ is the vapor pressure deficit. At the daily time step, G is set to zero following standard FAO-56 practice, as the daily net heat exchange with the soil is negligible. Actual vapor pressure e_a is estimated as $e_a = (RH_{mean}/100) \cdot e_s$, where e_s is the mean of the saturation vapor pressures at daily maximum and minimum temperature — a simplification imposed by the available meteorological forcing, which provides only mean daily relative humidity.

The crop coefficient K_c scales ET_0 to the actual vegetation type and phenological stage. Under non-limiting soil moisture, crop evapotranspiration is:

$$ET_c = K_c \cdot ET_0 \tag{3.2}$$

When the soil moisture falls below a threshold s_1, stomatal conductance decreases and actual evapotranspiration is reduced proportionally [8]:

$$ET = \min\left(1, \frac{s}{s_1}\right) \cdot K_c \cdot ET_0 \tag{3.3}$$

where s is the degree of saturation and ET_0 is expressed in mm/day. The threshold s_1 is a free parameter estimated through calibration.

3.1.2 Snow Accumulation and Melt

Given the elevation range of the Cordevole basin — from 700 to over 3300 m a.s.l. — snow dynamics play a decisive role in the seasonal water balance. RHYME incorporates a temperature-index (degree-day) snow module [7], which uses air temperature as the sole forcing variable. This is a common and practical choice for semi-distributed models operating in data-scarce mountain environments, where distributed radiation or energy balance data are rarely available.

Precipitation is partitioned into rainfall and snowfall by comparing mean daily temperature T_{ave} against a threshold T_{snow}: when $T_{ave} < T_{snow}$, precipitation is stored as snow and increasing the snow water equivalent H_{snow}. Melt onset is governed by a separate threshold T_{melt}, which need not coincide with T_{snow} — the temperature at which a snowpack begins to release meltwater can differ from the rain-snow transition temperature. When T_{ave} exceeds T_{melt}, the melt rate M_s is proportional to the positive temperature anomaly, but cannot exceed the available snowpack:

$$M_s = \min\left(\frac{H_{snow}}{\Delta t}, \max\left[0, \alpha_{melt}\left(T_{ave} - T_{melt}\right)\right]\right) \tag{3.4}$$

where α_{melt} is the degree-day melt factor (mm d^{-1} °C^{-1}) and Δt is the computational time step. Both T_{snow}, T_{melt}, and α_{melt} are free parameters estimated through calibration.

The total liquid water input reaching the soil surface combines the rainfall fraction with snowmelt:

$$J_{tot} = J - J_{snow} + M_s \tag{3.5}$$

where J is total precipitation, J_{snow} is the snowfall fraction withheld from the soil balance and stored in the snowpack.

3.1.3 Soil Moisture Balance and Runoff Generation

At each time step, the liquid water flux J_{tot} reaching the soil surface is partitioned between infiltration I and surface runoff R. Infiltration is limited by three concurrent constraints: the incoming flux itself, a maximum infiltration capacity $I_{\max}$, and the available storage capacity of the root zone:

$$I = \min\left[J_{tot}, I_{\max}, \frac{(1-s)\cdot n \cdot Z_r}{\Delta t}\right] \tag{3.6}$$

where s is the degree of saturation, n is soil porosity, and Z_r is root zone depth. Surface runoff is simply the fraction that cannot infiltrate:

$$R = J_{tot} - I. \tag{3.7}$$

A portion of the infiltrated water percolates beyond the root zone as deep drainage L, modelled as a power function of saturation:

$$L = K_0 \cdot s^c \tag{3.8}$$

where K_0 is the saturated hydraulic conductivity and c is a nonlinearity exponent. For $c = 1$ the drainage response is linear; for $c \gg 1$ it becomes strongly threshold-like, with negligible percolation at low saturation and a sharp increase as the soil approaches field capacity. The calibrated value $c \approx 12$ places the Cordevole basin firmly in the latter regime.

The evolution of soil moisture is governed in continuous form by the root-zone water balance:

$$\frac{ds}{dt} = \frac{1}{n \cdot Z_r} (I - L - ET) \tag{3.9}$$

In the numerical implementation, this equation is not integrated simultaneously for all fluxes. Instead, an operator-splitting scheme is applied: infiltration, drainage, and evapotranspiration are computed and applied sequentially within each time step, with the saturation state updated after each operation. This approach reduces mass balance errors that would otherwise accumulate when saturation changes rapidly within a single step.

3.1.4 Linear Reservoir Scheme

Hillslope fluxes are converted into discharge at the sub-catchment outlet through four conceptual linear reservoirs arranged in parallel, each representing a distinct flow pathway with its own characteristic response time:

- *Urban reservoir* (S_{urb}): receives direct runoff from impervious surfaces, scaled by an effective runoff coefficient c_d;
- *Surface reservoir* (S_{sup}): receives surface runoff R from the pervious fraction of the catchment;
- *Rapid subsurface reservoir* (S_{rap}): receives a fraction α of the leaching flux L, representing fast preferential flow pathways;
- *Deep reservoir* (S_{prof}): receives the fraction $(1-\alpha)\beta$ of the leaching flux, governing baseflow. The remaining fraction $(1-\alpha)(1-\beta)L$ is routed to deep groundwater recharge and excluded from the simulated streamflow.

Each reservoir drains linearly:

$$Q_k = K_k \cdot S_k, \qquad K_k = \min\left(\frac{1}{\Delta t}, \frac{1}{t_k}\right) \tag{3.10}$$

where t_k is the response time of reservoir k. The upper bound $1/\Delta t$ on the drainage coefficient ensures that no reservoir can empty faster than one time step, which is required for numerical stability. Total hillslope discharge is the sum of the four contributions.

3.1.5 Geomorphological Routing

Network routing in RHYME is based on the geomorphological Instantaneous Unit Hydrograph (IUH), which avoids the computational cost of solving the full Saint-Venant equations by convolving the hillslope hydrograph with a transfer function derived from the advection-dispersion equation. For a reach of length ℓ, the IUH takes the form [12]:

$$f(t) = \frac{\ell}{\sqrt{4\pi D_h t^3}} \exp\left(-\frac{(\ell - ut)^2}{4D_h t}\right) \tag{3.11}$$

where u is the effective wave celerity and D_h is the hydrodynamic dispersion coefficient. Together they control the translation and spreading of the flood wave along each channel segment. In this work, both parameters are treated as fixed basin-wide constants, derived from a dedicated HEC-RAS simulation rather than estimated through calibration — an approach described in Chapter 5.

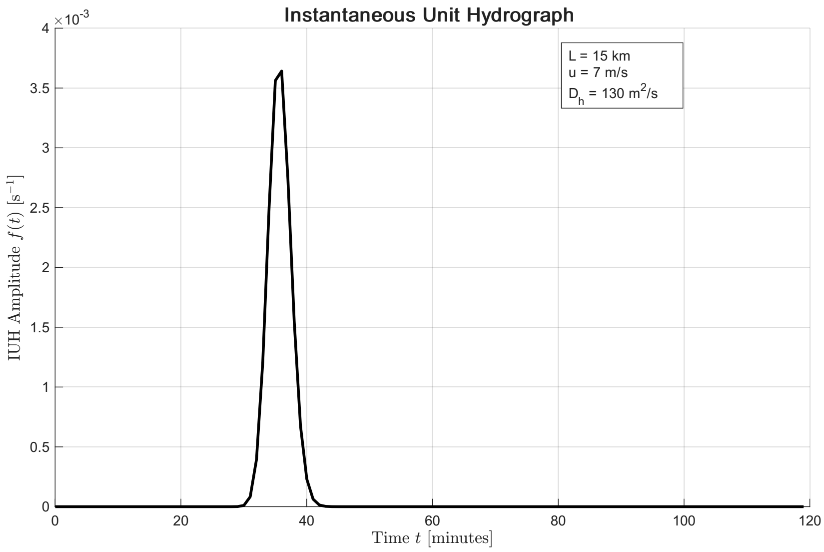

Figure 3.2: Instantaneous Unit Hydrograph (IUH) derived from the advection-dispersion equation for a representative 15 km reach, computed with the routing parameters adopted in RHYME ($u = 7$ m/s, $D_h = 130$ m^2/s).

The routed discharge at any downstream point is obtained by convolving the sub-catchment hillslope hydrograph $Q_{hill}(t)$ with the IUH:

$$Q_{routed}(t) = \int_0^t Q_{hill}(\tau)\, f(t-\tau)\, d\tau \tag{3.12}$$

In practice, $f(t)$ is discretised at intervals of Δt and truncated once the cumulative mass reaches 99.9% of the unit volume. The kernel is then renormalised to ensure exact mass conservation despite the truncation.

Three routing configurations are available, selected via a model flag. The first propagates runoff instantaneously to the outlet with no routing kernel applied; it is used only for testing. The second routes each sub-catchment hydrograph directly to the basin outlet through a single convolution over channel distance L_{out}; this is the configuration used in the calibration presented here, as it is computationally efficient and well suited to single-outlet simulations. The third performs sequential reach-by-reach routing, combining upstream contributions at each node before propagating further downstream; this preserves the full spatial distribution of discharge and is the configuration used in the operational mode, where intermediate-node estimates are required.

The main limitation of the approach lies in the assumption of constant u and D_h. In

Alpine catchments, wave celerity increases substantially with discharge, so this simplification may introduce timing errors during high-magnitude events. Addressing this limitation — at least for the main Cordevole stem — is one of the motivations for the HEC-RAS analysis presented in the next chapter.

3.2 The HEC-RAS Hydraulic Model

The geomorphological IUH routing assumes constant wave celerity, which is a reasonable approximation for network-scale simulations but cannot capture the nonlinear wave dynamics that characterize high-discharge events in confined Alpine channels. To derive physically consistent routing parameters for the main Cordevole stem, a one-dimensional hydraulic model was set up in HEC-RAS (Hydrologic Engineering Center's River Analysis System, [2]).

HEC-RAS solves the De Saint-Venant equations for unsteady, one-dimensional flow, expressing conservation of mass and momentum:

$$\frac{\partial A}{\partial t} + \frac{\partial Q}{\partial x} = q_l \tag{3.13}$$

$$\frac{\partial Q}{\partial t} + \frac{\partial}{\partial x}\left(\frac{Q^2}{A}\right) + gA\left(\frac{\partial z}{\partial x} + S_f\right) = 0 \tag{3.14}$$

where A is the wetted cross-sectional area, Q is the discharge, q_l is the lateral inflow per unit length, z is the water surface elevation, g is gravitational acceleration, and S_f is the friction slope, evaluated using Manning's equation:

$$S_f = \frac{n^2 Q^2}{A^2 R^{4/3}} \tag{3.15}$$

This formulation resolves flood wave attenuation, cross-sectional geometry changes, and discharge-dependent nonlinearities that a constant-celerity IUH cannot represent.

A 1D approach is appropriate here: in the Cordevole valley, flow is strongly confined by the narrow channel geometry, and a 2D model would introduce substantial data requirements without a commensurate gain in accuracy for the purpose of routing parameter estimation.

3.3 Model Calibration and Parameter Uncertainty

Several parameters of RHYME — including soil hydraulic properties, reservoir residence times, and snow thresholds — cannot be measured directly and must be inferred from observed discharge. Rather than seeking a single optimal parameter set, a Bayesian framework is adopted, which yields a full posterior distribution over the parameter space and allows uncertainty to be propagated explicitly through model predictions.

3.3.1 Bayesian Inference and Likelihood Function

The Bayesian framework combines three elements. The prior probability distribution $p(\theta)$ encodes available knowledge about the parameters before any discharge data are considered. For parameters lacking independent measurements, a uniform prior over the physically plausible range is assigned, expressing only that the parameters must lie within known physical bounds. For three parameters with literature constraints — s_1, T_{melt}, and T_{snow} — informative Gaussian priors are used instead.

The likelihood $L(\theta \mid \mathbf{Y})$ quantifies how well the model reproduces the observed hydrograph given a parameter set θ. Assuming independent, normally distributed residuals with standard deviation σ (itself treated as a calibration parameter):

$$\ln L(\theta|\mathbf{Y}) = -\frac{N}{2}\ln(2\pi\sigma^2) - \frac{1}{2\sigma^2}\sum_{i=1}^{N}\left[Y_i - \hat{Y}_i(\theta)\right]^2 \tag{3.16}$$

where N is the number of retained observations, Y_i is measured discharge, and $\hat{Y}_i(\theta)$ is the corresponding model output. The normality assumption is a simplification: discharge residuals are typically heteroscedastic, with variance growing at high flows. A Gaussian likelihood therefore weights all residuals equally and tends to favour solutions that minimize average error rather than peak reproduction.

The posterior distribution $p(\theta|\mathbf{Y})$ follows from Bayes' theorem:

$$p(\theta|\mathbf{Y}) \propto L(\theta|\mathbf{Y})p(\theta) \tag{3.17}$$

3.3.2 The DREAM Algorithm

Direct evaluation of the posterior is intractable for a 16-dimensional parameter space. The DiffeRential Evolution Adaptive Metropolis algorithm (DREAM, [14]) is used instead, which samples the posterior through a population of parallel Markov chains that exchange information via differential evolution moves.

At each iteration, a candidate parameter vector is proposed for chain i by drawing two other chains a and b at random and computing:

$$\theta^* = \theta_i + \gamma\,(\theta_a - \theta_b) + \varepsilon \tag{3.18}$$

where γ is a scaling factor and ε is a small stochastic perturbation included to ensure ergodicity. The candidate θ^* is accepted with probability:

$$p_{acc} = \min\left(1,\ \frac{p(\theta^* \mid Y)}{p(\theta_i \mid Y)}\right) \tag{3.19}$$

Moves that increase the posterior probability are always accepted; moves that decrease it are accepted with probability equal to the posterior ratio. This guarantees that the chain converges asymptotically to the target distribution. The differential evolution proposal is particularly effective when posterior correlations are strong or the geometry is non-standard, which is common in hydrological calibration problems.

Convergence is assessed using the Gelman-Rubin statistic $\hat{R}$ [5], computed periodically across all chains. Once $\hat{R} \lesssim 1.01$ for all parameters, the chains are considered mixed and the burn-in portion is discarded before computing posterior statistics.

Chapter 4

Crop Coefficient and Evapotranspiration Estimation

4.1 Land Cover Classification

Land cover data for the Cordevole basin were extracted from the CORINE Land Cover (CLC) dataset [3] compiled for the full Piave network, and filtered to the 42 sub-catchments that make up the model domain closed at Ponte Mas. Table 4.1 reports the area-weighted fractional composition by CLC class; Figure 4.1 shows the spatial distribution across sub-catchments.

Table 4.1: CORINE Land Cover classes present in the Cordevole basin, with area fraction computed as the sub-catchment area-weighted average (42 sub-catchments, total area 700.3 km^2).

CLC code	**Class name**	**Area fraction (%)**
111	Continuous urban fabric	1.45
112	Discontinuous urban fabric	0.05
131	Mining areas	0.02
231	Pastures	3.73
242	Complex cultivation patterns	0.10
243	Agricultural land with vegetation	1.01
311	Broad-leaved forest	7.50
312	Coniferous forest	33.52
313	Mixed forest	9.35
321	Natural Grasslands	13.79
322	Moors and heathland	9.70
324	Transitional woodland-shrub	0.56
331	Beaches, dunes, sands	0.32
332	Bare rocks	9.47
333	Sparsely vegetated areas	9.27
335	Glaciers and perpetual snow	0.07
512	Water bodies	0.07

The basin is strongly dominated by natural and semi-natural land. Forest (CLC 311, 312, 313) covers 50.37% of the total area, with coniferous forest alone (312) accounting for a third of the basin. High altitude natural classes — grasslands, heathland, bare rock, and sparse vegetation (321, 322, 332, 333) — add a further 42.23%. Urban and agricultural land together represent less than 3%, confined to the valley floors around Agordo and along the lower Cordevole reach. This distribution is consistent with the geological and topographic description of Section 2.3 and underscores the importance of a spatially distributed, seasonally varying crop coefficient for accurate evapotranspiration modelling.

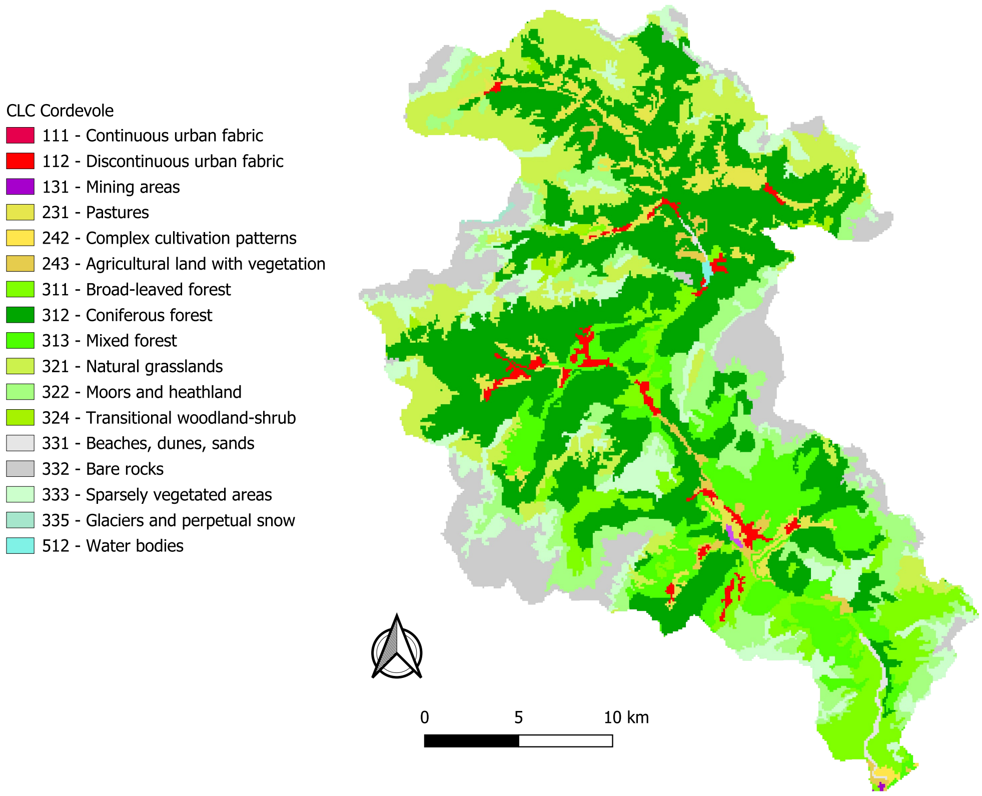

Figure 4.1: CORINE Land Cover classification of the Cordevole basin, overlaid on the 42 sub-catchment boundaries of the RHYME model domain.

4.2 Monthly Crop Coefficient Computation

In the original RHYME configuration, K_c was a single scalar parameter, spatially uniform and constant throughout the year. The updated implementation, replaces it with a monthly, sub-catchment-specific field derived from the land cover composition of each unit.

The land cover matrix F $(N_{sc} \times N_{class})$ contains the fractional area of each CLC class within each sub-catchment of the Piave network. It is computed once for the full network and subset at run time to the 42 sub-catchments relevant to the current simulation domain. Monthly K_c values per CLC class were taken from [10], who provide four seasonal coefficients — initial (March–May), mid-season (June–August), late-season (September–October), and cold season (November–February) — which were assigned uniformly to each month within the corresponding season, yielding a reference matrix K of dimensions $N_{class} \times 12$. The resulting values for the classes present in the Cordevole basin are reported in Table 4.2.

Table 4.2: Monthly crop coefficients for the CLC classes present in the Cordevole basin, derived from the seasonal values of [10].

CLC	Jan	Feb	Mar	Apr	May	Jun	Jul	Aug	Sep	Oct	Nov	Dec
111	0.00	0.00	0.20	0.20	0.20	0.40	0.40	0.40	0.25	0.25	0.00	0.00
112	0.00	0.00	0.10	0.10	0.10	0.30	0.30	0.30	0.20	0.20	0.00	0.00
131	0.00	0.00	0.16	0.16	0.16	0.36	0.36	0.36	0.26	0.26	0.00	0.00
231	0.00	0.00	0.40	0.40	0.40	0.90	0.90	0.90	0.80	0.80	0.00	0.00
242	0.00	0.00	1.10	1.10	1.10	1.35	1.35	1.35	1.25	1.25	0.00	0.00
243	0.00	0.00	0.70	0.70	0.70	1.15	1.15	1.15	1.00	1.00	0.00	0.00
311	0.60	0.60	1.30	1.30	1.30	1.60	1.60	1.60	1.50	1.50	0.60	0.60
312	1.00	1.00	1.00	1.00	1.00	1.00	1.00	1.00	1.00	1.00	1.00	1.00
313	0.80	0.80	1.20	1.20	1.20	1.50	1.50	1.50	1.30	1.30	0.80	0.80
321	0.00	0.00	0.30	0.30	0.30	1.15	1.15	1.15	1.10	1.10	0.00	0.00
322	0.00	0.00	0.80	0.80	0.80	1.00	1.00	1.00	0.95	0.95	0.00	0.00
324	0.00	0.00	0.80	0.80	0.80	1.00	1.00	1.00	0.95	0.95	0.00	0.00
331	0.00	0.00	0.20	0.20	0.20	0.30	0.30	0.30	0.25	0.25	0.00	0.00
332	0.00	0.00	0.15	0.15	0.15	0.20	0.20	0.20	0.05	0.05	0.00	0.00
333	0.00	0.00	0.40	0.40	0.40	0.60	0.60	0.60	0.50	0.50	0.00	0.00
335	0.48	0.48	0.48	0.48	0.48	0.52	0.52	0.52	0.52	0.52	0.48	0.48
512	0.00	0.00	0.25	0.25	0.25	0.65	0.65	0.65	1.25	1.25	0.00	0.00

The sub-catchment K_c matrix is then obtained by matrix multiplication:

$$K_c = F \cdot K \tag{4.1}$$

Each entry of the resulting $N_{sc} \times 12$ matrix is the area-weighted average crop coefficient for sub-catchment i in month m:

$$K_{c,i,m} = \sum_{j=1}^{N_{class}} F_{ij} \cdot K_{jm} \tag{4.2}$$

Before executing the multiplication, three alignment checks are performed automatically: the CLC class codes in the land-cover file must match the code sequence in the K_c reference table; the K_c table must contain exactly 12 columns; and the sub-catchment IDs must correspond to the internal node ordering of the model geometry. If any check fails, the code raises an error and halts. This prevent silent misalignment between the land-cover and crop-coefficient matrices, which would produce incorrect K_c values without any obvious numerical symptom.

4.3 Spatial and Seasonal Kc Results

Table 4.3 reports the basin-average monthly K_c, computed as the area-weighted mean across the 42 sub-catchments.

Table 4.3: Basin-averaged monthly crop coefficient for the Cordevole basin (area-weighted mean across the 42 sub-catchments).

Jan	Feb	Mar	Apr	May	Jun	Jul	Aug	Sep	Oct	Nov	Dec
0.455	0.455	0.746	0.746	0.746	0.984	0.984	0.984	0.916	0.916	0.455	0.455

The seasonal signal is clear. The cold-season value (0.455, November–February) reflects the dominance of coniferous forest (CLC 312), which retains a year-round K_c of 1.0 according to [10] but is diluted by the large fraction of bare rock, sparse vegetation, and grasslands that carry zero cold-season coefficients. The mid-season peak (0.984, June–August) is reached when deciduous and herbaceous classes reach full canopy development. The annual mean is 0.737, compared to a calibrated scalar of approximately 1.0 used in the baseline rhyme2023 — an effective overestimation of evaporative demand that is partially absorbed by the calibrated parameter set of that version.

Figure 4.2 shows the spatial distribution of K_c in January and July. The contrast between the two maps captures both dimensions of the heterogeneity introduced by the updated formulation: the seasonal amplitude, which ranges from near-zero to near-unity depending on the class, and the spatial pattern, which follows the elevation-driven land cover gradient described in Section 2.3.

4.4 Evapotranspiration: Updated FAO-56 Implementation

The baseline model computed ET_0 using a simplified temperature-based routine. In rhyme2026, this is replaced by the FAO-56 Penman-Monteith equation [1], applied daily and independently for each sub-catchment using spatially distributed meteorological inputs: minimum and maximum daily temperature (T_{min},T_{max}), mean temperature (T_{med}), mean relative humidity, wind speed at 2 m height, and incoming solar radiation. The resulting ET_0 field has dimensions $N_{day} \times N_{sc}$.

At each hourly time step, actual evapotranspiration is computed by combining the daily ET_0 field with the monthly crop coefficient and the soil moisture limitation factor.

$$ET = \min\left(1, \frac{s}{s_1}\right) \cdot K_{c,m} \cdot \frac{ET_0}{86400} \tag{4.3}$$

where s is the current saturation degree, s_1 is the water stress threshold, $K_{c,m}$ is the crop coefficient for the current month, and the factor 1/86400 converts ET_0 from mm/day to mm/s, the standard unit used in the code. The daily ET_0 value is held constant across all 24 hourly steps of the corresponding day.

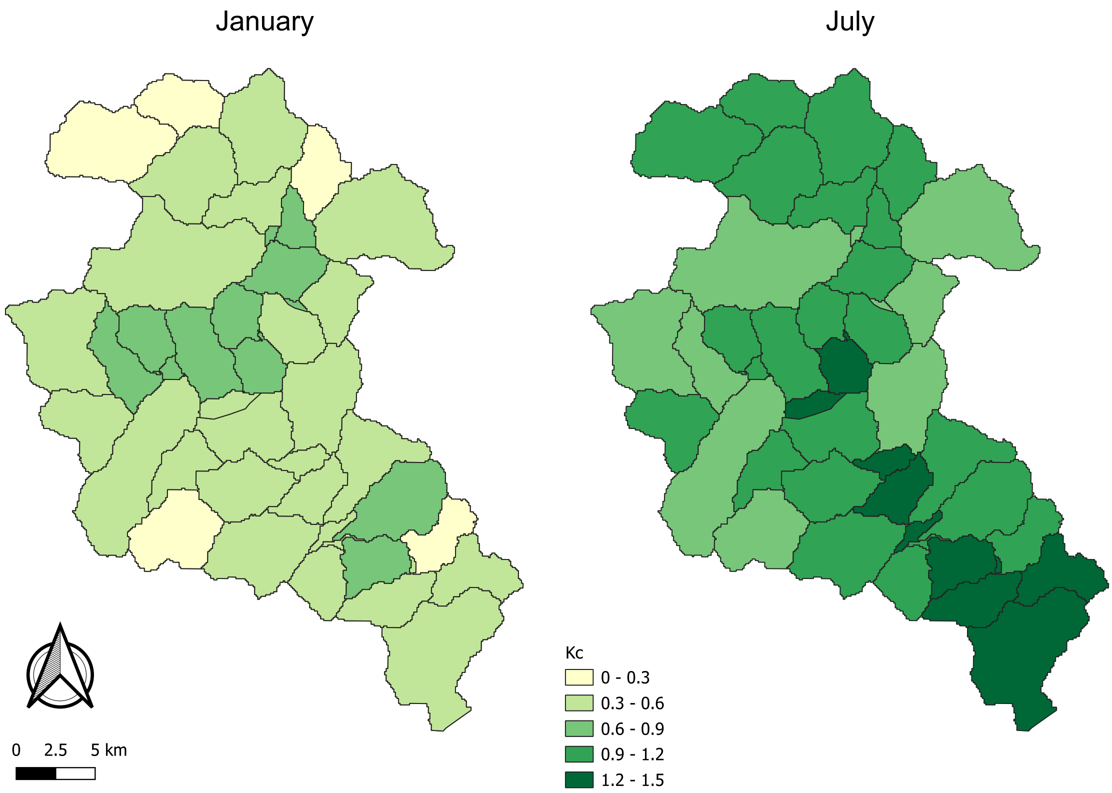

Figure 4.2: Spatial distribution of K_c across the 42 Cordevole sub-catchments for January (left) and July (right). The contrast between the two months reflects both the seasonal amplitude of the crop coefficients and the elevation-driven land cover gradient of the basin.

4.5 Comparison with the Original ET_0 Routine

The two ET_0 series — original simplified Penman-Monteith and updated FAO-56 — were compared over the 1996–2019 period using basin-averaged daily values, area-weighted across the 42 sub-catchments. Figure 4.3 shows the full record.

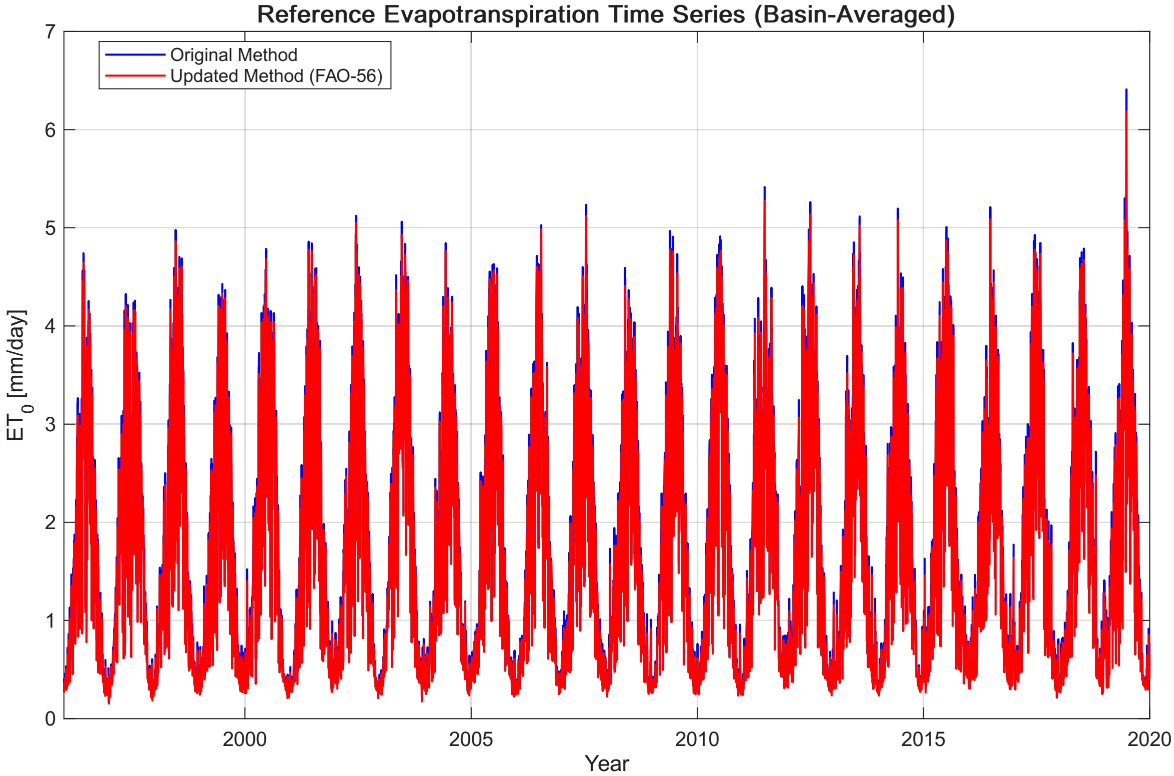

Figure 4.3: Basin-averaged daily ET_0 over 1996–2019, comparing the original simplified routine and the updated FAO-56 Penman-Monteith implementation.

The two series are in close agreement ($R = 0.997$), but the original routine is uniformly higher than the FAO-56 estimate. The mean bias equals the mean absolute error (BIAS = MAE = 0.056 mm/day), confirming that the sign of the difference never reverses over the entire record: the original method systematically overestimates ET_0 relative to the Penman-Monteith reference. The RMSE is 0.068 mm/day, and the maximum single-day discrepancy is 0.267 mm/day — modest relative to the summer peaks exceeding 5 mm/day visible in Figure 4.3. The systematic offset reflects the correction terms for radiation, wind speed, humidity, elevation, and atmospheric pressure that the FAO-56 formulation incorporates and the original routine does not.

Figure 4.9 compares the monthly linear trends over the same period. Ten of the twelve months show a positive trend in both methods; February and May are the exceptions, with a negative trend of similar magnitude in both series. The FAO-56 estimates tend to show slightly smaller trend magnitudes than the original routine, most visibly in July and September, suggesting that the additional physical constraints of the Penman-Monteith equation modestly dampen the apparent long-term signal without altering its seasonal pattern.

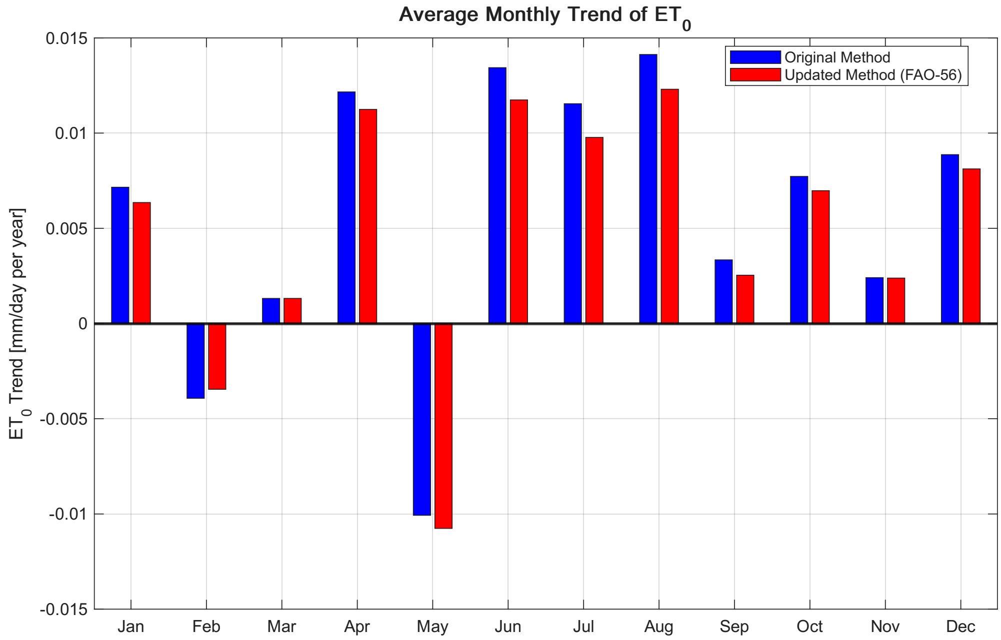

Figure 4.4: Monthly linear trend of basin-averaged ET_0 (mm/day per year), for the original routine and the FAO-56 implementation, 1996–2019.

4.6 Trends in Meteorological Drivers and $\mathbf{ET_0}$

Systematic long-term changes in the meteorological forcing can shift the water balance over time and bias parameter estimates if they occur within the calibration window. A secondary motivation for this analysis is to assess whether a climate change signal is detectable in the forcing record of the Cordevole basin, and whether such a signal has already influenced the long-term evaporative demand over the period considered. This section documents the trends observed in the 1996–2019 forcing record and uses them as an indirect consistency check on the updated FAO-56 ET_0 implementation: if the Penman-Monteith formulation correctly represents the dominant physical drivers, the ET_0 trend should be consistent with the individual trends in temperature, wind speed, radiation, and humidity.

Basin-averaged daily series were obtained by area-weighting the sub-catchment fields across the 42 Cordevole sub-catchments. For each variable — FAO-56 ET_0, mean air temperature (T_{med}), solar radiation (R_s), wind speed (v_v), and relative humidity (RH) — a linear model was fitted to the yearly seasonal mean for each of the four standard meteorological seasons (DJF, MAM, JJA, SON) using `fitlm`. Statistical significance was assessed from the p-value of the slope. Results are summarized in Table 4.4.

Wind speed is the most consistent signal in the record: it increases significantly in all four seasons ($p < 0.001$ in DJF, MAM and JJA; $p = 0.002$ in SON), with the trend visible across the full record (Figure 4.5). Temperature shows significant warming in

Table 4.4: Statistical significance (p-value) of seasonal linear trends in meteorological variables and ET_0, 1996–2019. Asterisks indicate significance at the 5% level.

Season	ET_0	T_{med}	R_s	v_v	RH
Winter (DJF)	0.046*	0.398	0.027*	0.000*	0.854
Spring (MAM)	0.925	0.170	0.383	0.000*	0.649
Summer (JJA)	0.088	0.006*	0.470	0.000*	0.801
Autumn (SON)	0.130	0.004*	0.820	0.002*	0.488

summer and autumn ($p = 0.006$ and $p = 0.004$; (Figure 4.6); the winter and spring trends are of similar visual magnitude but do not reach significance, likely because cold-season interannual variability is higher. Solar radiation trends in the opposite direction in winter ($p = 0.027$, negative), while the other three seasons show no detectable trend (Figure 4.7). Relative humidity is flat in all seasons (Figure 4.8): the year-to-year scatter dominates, and no significant directional change is detectable over the record.

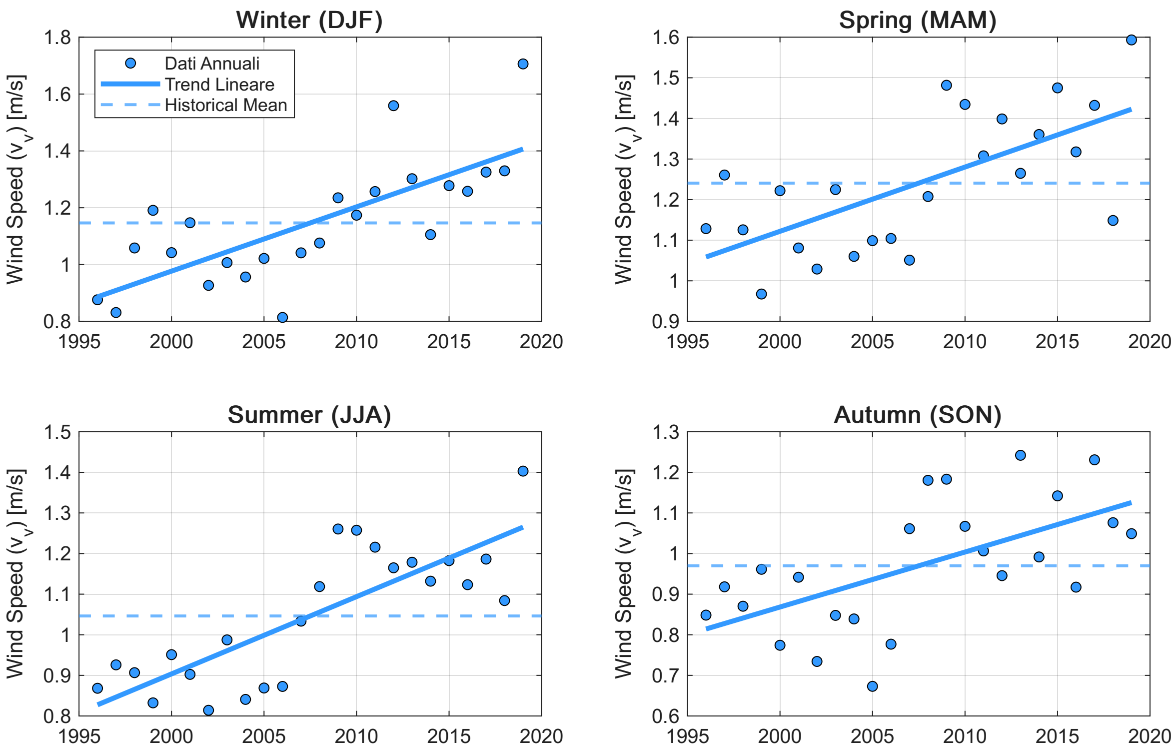

Figure 4.5: Seasonal evolution of basin-averaged wind speed (v_v), 1996–2019, with fitted linear trend and historical mean.

The ET_0 trends and the corresponding total percentage changes over the 24-year record are shown in Figure 4.9 and Table 4.5. The percentage change is computed as slope × 24 years, normalized by the seasonal historical mean.

The largest relative change occurs in winter (+17–18% for both methods), but this should not be overinterpreted: winter ET_0 values are very low in absolute terms, so even a small absolute trend produces a large percentage. The significant p-value for

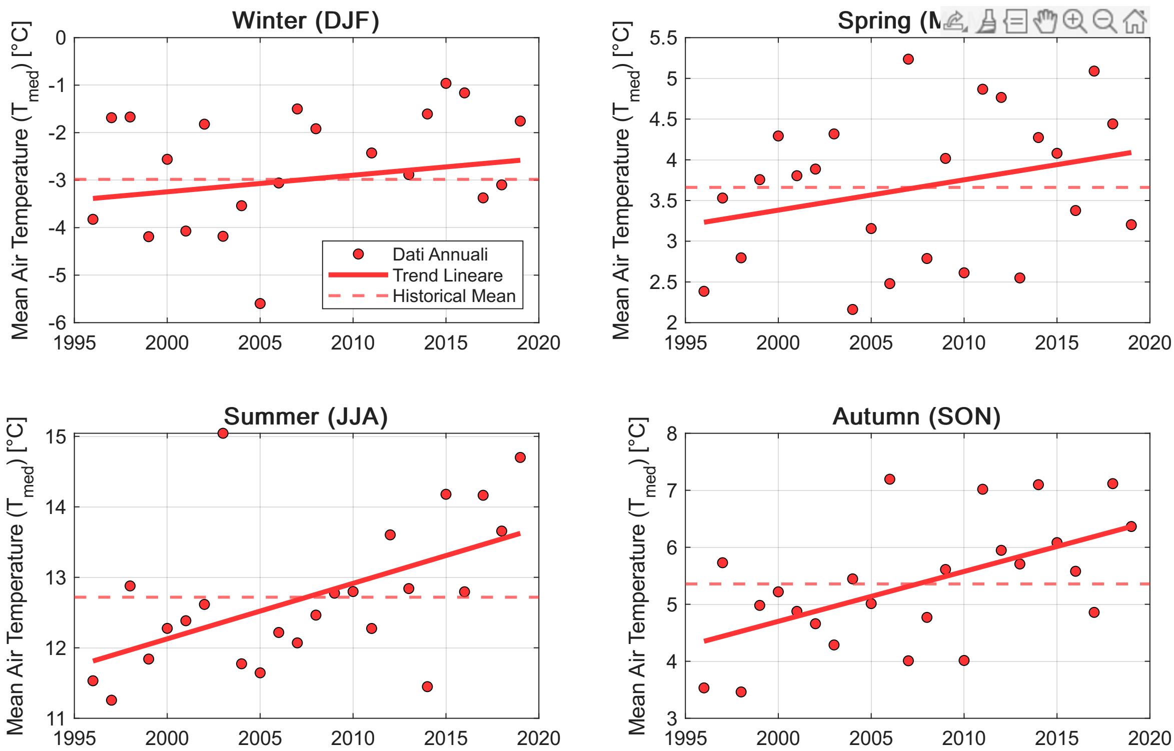

Figure 4.6: Seasonal evolution of basin-averaged mean temperature (T_{med}), 1996–2019, with linear fitted trend and historical mean.

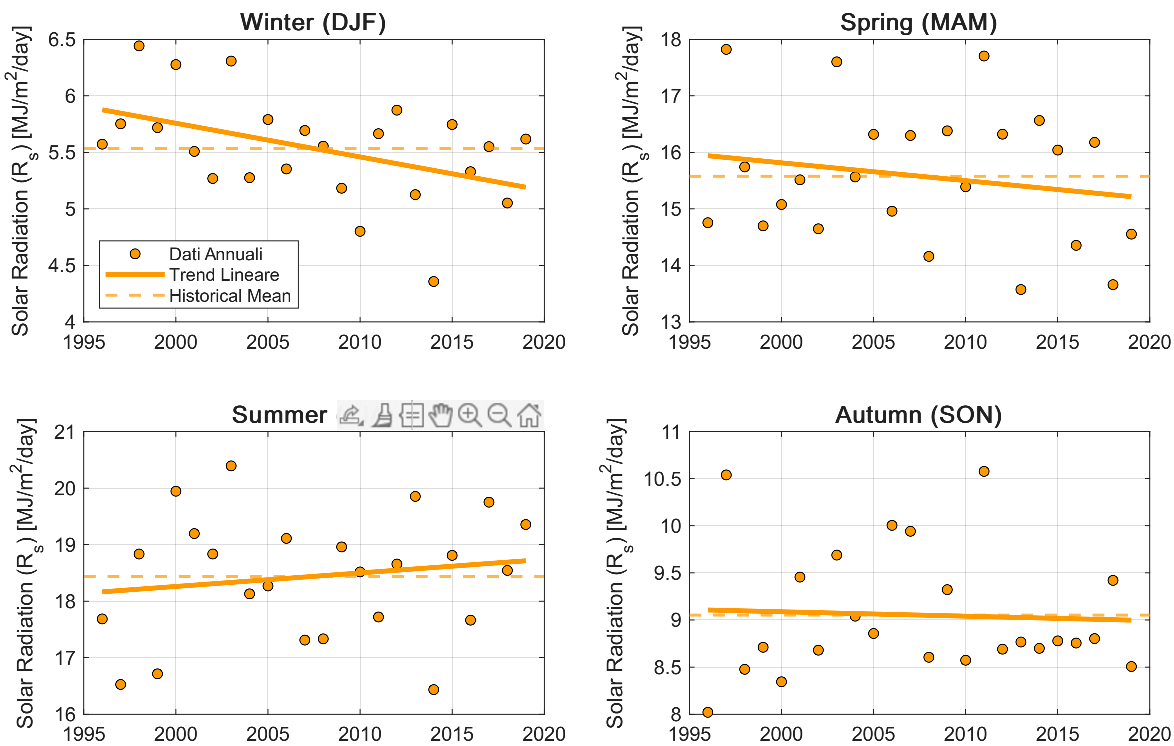

Figure 4.7: Seasonal evolution of basin-averaged solar radiation (R_s), 1996–2019, with linear fitted trend and historical mean.

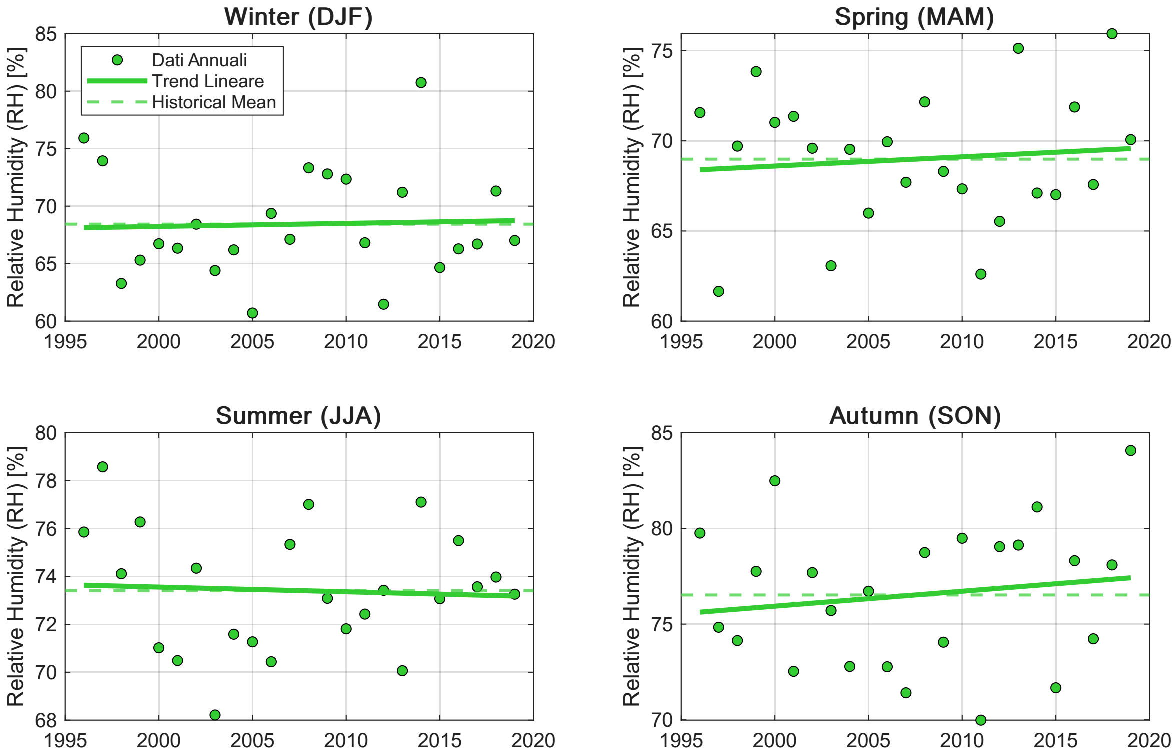

Figure 4.8: Seasonal evolution of basin-averaged relative humidity (RH), 1996–2019, with linear fitted trend and historical mean.

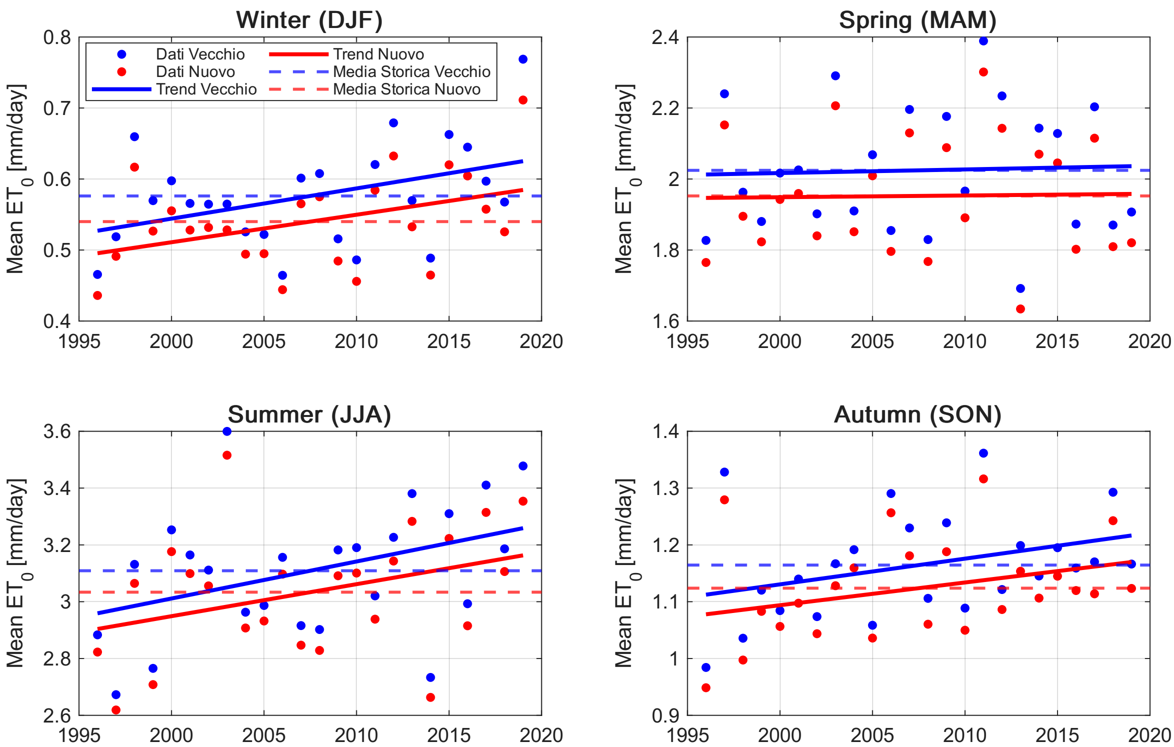

Figure 4.9: Seasonal evolution of basin-averaged ET_0, 1996–2019, for the original routine and the FAO-56 implementation, with linear trends and historical means.

Table 4.5: Total percentage change in seasonal ET_0 over 1996–2019 (24-years), for the original routine and the FAO-56 implementation.

Season	**Original (%)**	**FAO-56 (%)**
Winter (DJF)	17.64	17.22
Spring (MAM)	1.21	0.60
Summer (JJA)	10.06	8.91
Autumn (SON)	9.33	8.54

winter ($p = 0.046$) is consistent with this — the trend is detectable, but modest in magnitude. Summer and autumn increases (9–10%) are driven by the combination of significant warming and rising wind speed, both of which enhance the Penman-Monteith demand. Spring is nearly neutral, with no significant trend in any of its drivers.

The FAO-56 series shows systematically smaller percentage changes than the original routine in every season, consistent with the negative bias identified in Section 4.5. Taken together, the dominant signal in the forcing record is an increase in wind speed that affects all seasons, with a secondary warming contribution in summer and autumn. The cumulative effect is a gradual increase in evaporative demand that, if sustained beyond the calibration period, would tend to reduce runoff ratios and could shift the balance between the calibrated soil storage capacity $n \cdot Z_r$ and the evapotranspiration threshold s_1 if the model is applied under future conditions.

Chapter 5

The HEC-RAS Hydraulic Model

The geomorphological routing scheme described in Section 3.1.5 requires two basin-wide parameters, u and D_h, that cannot be measured directly and are difficult to constrain through hydrological calibration alone. This chapter describes the one-dimensional hydraulic simulation used to estimate them, covering the model domain, the reference flood event, and the parameter fitting procedure.

5.1 Model Domain and Cross-Section Extraction

The hydraulic model covers a 18.5 km reach of the lower Cordevole, from an upstream section near Agordo to the Ponte Mas gauging station (Figure 5.1). Cross-sections were extracted from a 5×5 m DTM and placed at the beginning (near Agordo) and at the end (coinciding with the dam in Ponte Mas) of the considered reach.

Manning's roughness coefficients were set to $n = 0.040$ $\mathrm{m}^{-1/3}\,\mathrm{s}$ for the main channel and $n = 0.060$ $\mathrm{m}^{-1/3}\,\mathrm{s}$ for the floodplain, following standard guidance for gravel-bed mountain streams with riparian vegetation.

5.2 Simulation of the September 1999 Flood Event

A one-dimensional unsteady simulation was run for the period 19–23 September 1999, one of the most significant flood events recorded in the Cordevole record. The upstream boundary was forced with the observed discharge hydrograph at the inlet; a normal depth condition was applied at Ponte Mas.

Figure 5.3 shows the resulting hydrographs at the two reach ends. The upstream peak reaches 625.6 m^3/s; the downstream peak at Ponte Mas is 617.6 m^3/s, an attenuation of 1.3%. The peak-to-peak travel time is 46 minutes.

5.3 Estimation of Routing Parameters u and D_h

Wave celerity u was estimated directly from the peak-to-peak travel time:

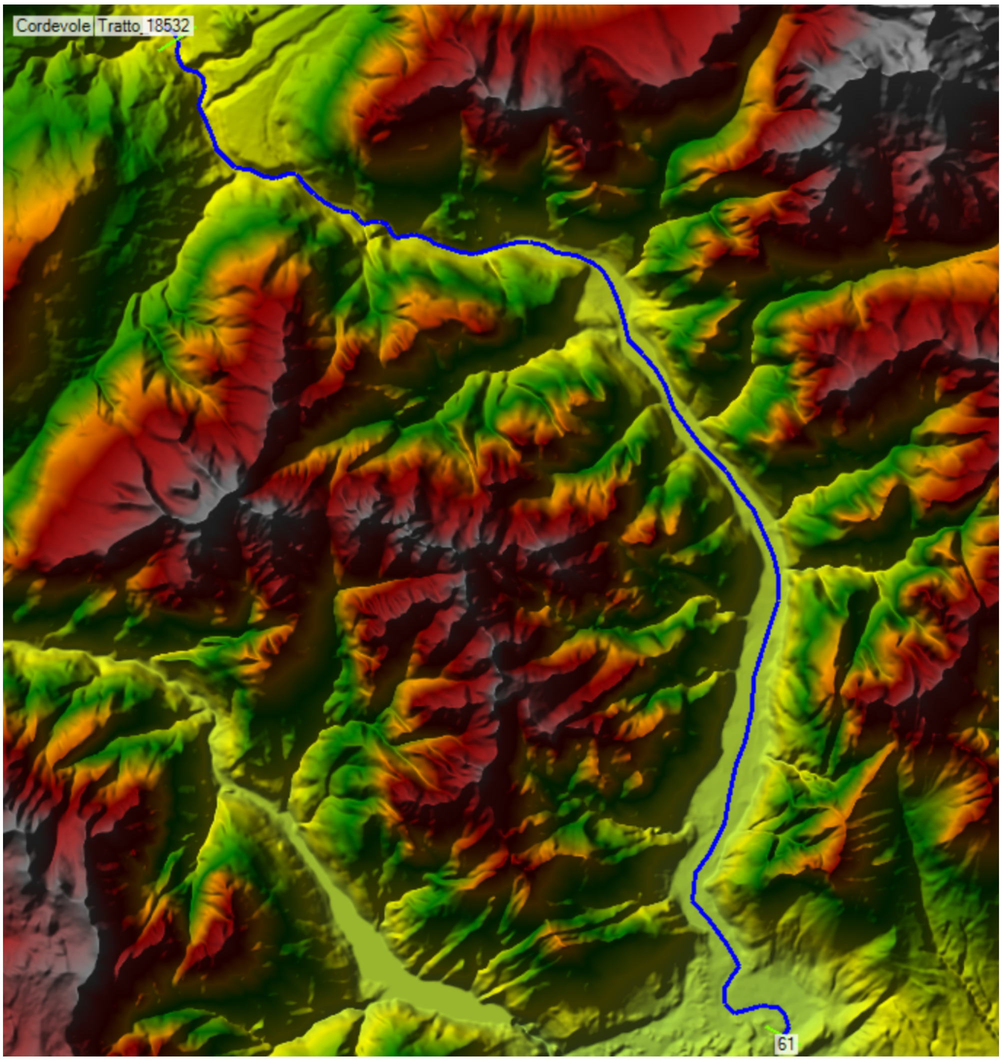

Figure 5.1: HEC-RAS model domain along the lower Cordevole reach (18.5 km), with the surveyed cross-sections locations.

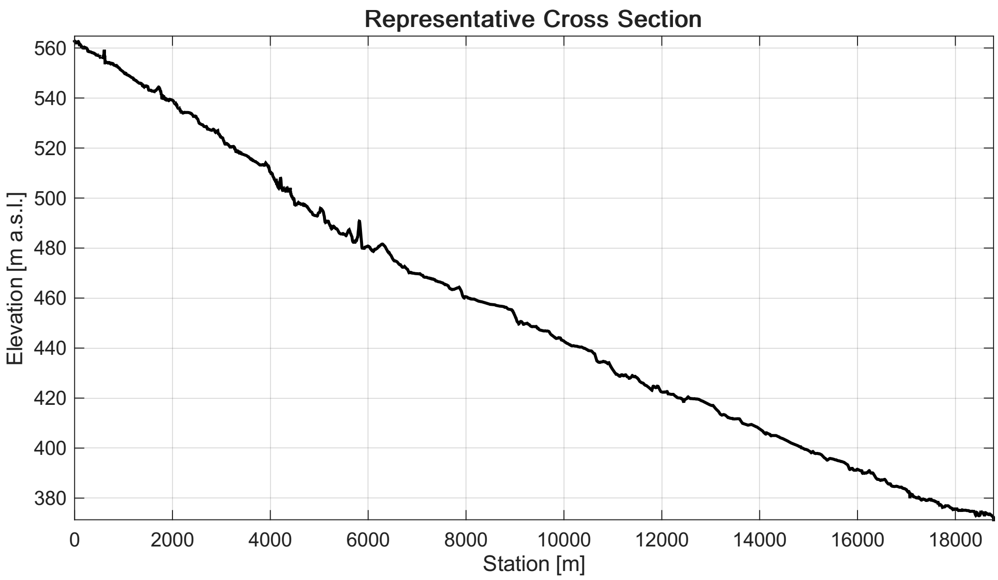

Figure 5.2: Longitudinal profile of the channel thalweg from the upstream boundary to Ponte Mas.

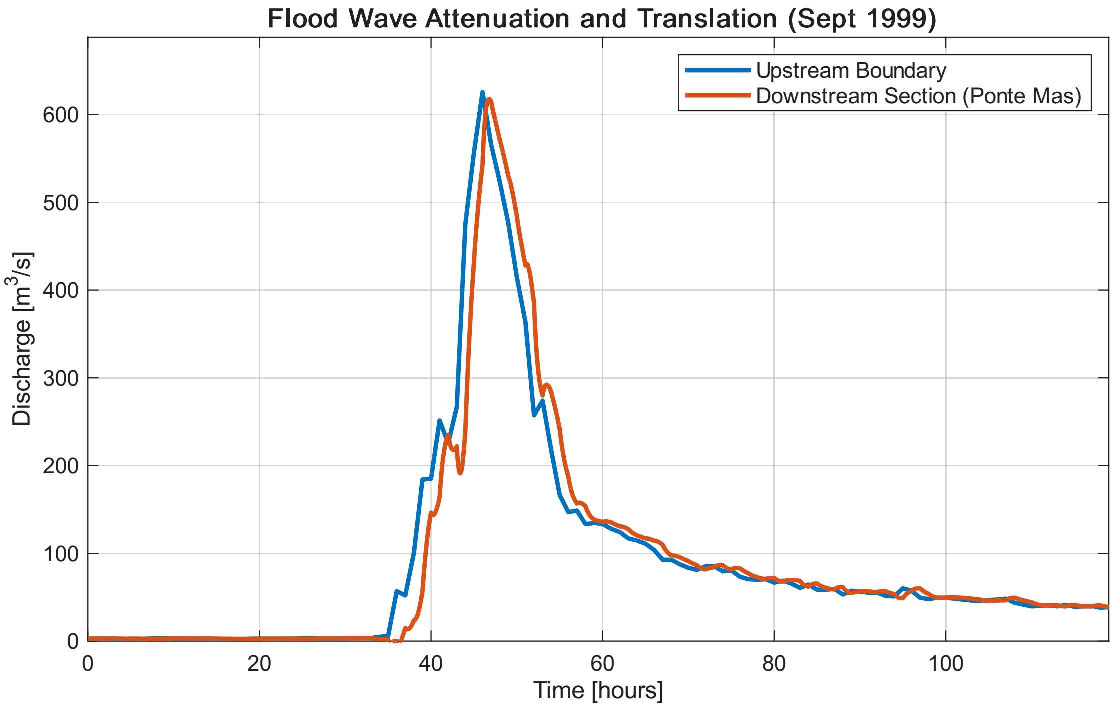

Figure 5.3: Upstream and downstream discharge hydrographs during the September 1999 reference event, showing the translation and attenuation of the flood wave over the 18.5 km reach.

$$u = \frac{L}{\Delta t_{peak}} = \frac{18471}{46 \times 60} \approx 6.69 \text{ m/s} \approx 7 \text{ m/s} \tag{5.1}$$

This kinematic estimate is independent of any optimization and provides a direct physical constraint on u. With u fixed at 7 m/s, the dispersion coefficient D_h was determined by minimizing the RMSE between the analytical advection-dispersion solution and the HEC-RAS downstream hydrograph:

$$Q^{pred}_{down}(t) = \int_0^t Q_{up}(\tau)\, f(t-\tau;\, u, D_h)\, d\tau \tag{5.2}$$

where f is the IUH kernel of Equation 3.11. A grid search over $D_h \in [50, 5000]$ m^2/s identifies a formal minimum at $D_h = 1530$ m^2/s (RMSE $= 16.338$ m^3/s), but the value $D_h = 130$ m^2/s adopted in RHYME yields a virtually identical fit quality (RMSE $=$ 16.345 m^3/s, NSE $= 0.984$; Figure 5.4). The RMSE surface is essentially flat with respect to D_h because advection dominates dispersion at this scale: the Péclet number $Pe = uL/D_h = 7 \times 18471/130 \approx 994 \gg 1$, indicating that wave translation is governed primarily by u and that D_h controls only the minor smoothing of the hydrograph shape. The value $D_h = 130$ m^2/s is therefore retained without modification.

The two parameters are assigned as fixed inputs to RHYME, reducing the calibration problem from 18 to 16 free parameters. The main limitation is the assumption of discharge-independent u and D_h: in Alpine channels, wave celerity increases with stage, so the estimated values are representative of high-flow conditions. Using a high-magnitude reference event for the fitting is therefore a deliberate choice, as the DREAM

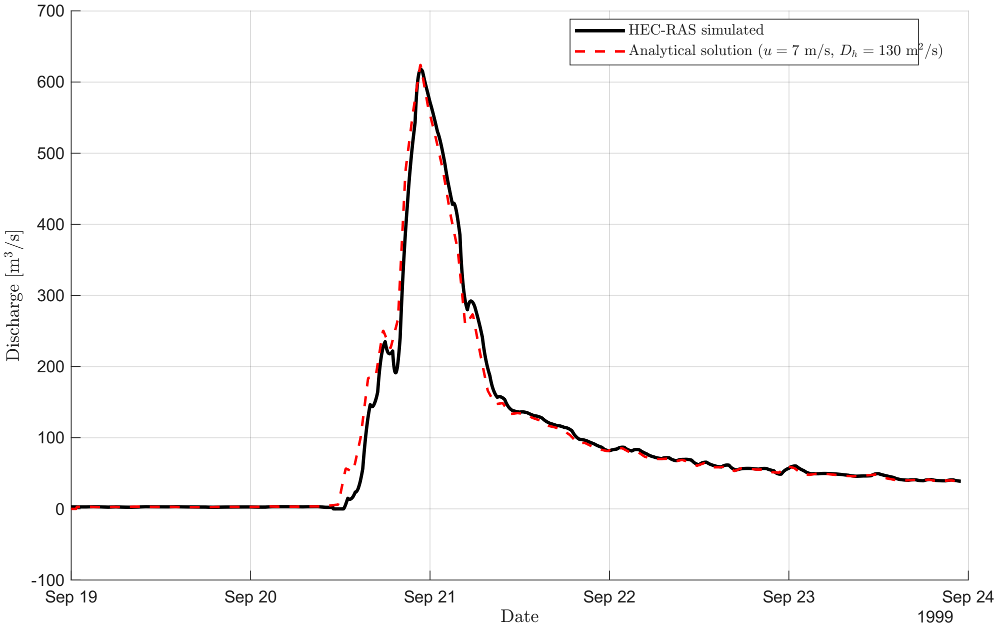

Figure 5.4: HEC-RAS downstream hydrograph at Ponte Mas and the analytical advection-dispersion solution with $u = 7$ m/s and $D_h = 130$ m^2/s, (NSE = 0.984).

calibration is driven primarily by flood peaks where routing accuracy has the greatest impact.

Chapter 6

Calibration and Validation Results

The rhyme2026 model was calibrated against observed discharge at the Ponte Mas gauging station over the period 1997–2012, with a one-year warm-up from January 1996 to reduce sensitivity to initial conditions. This chapter covers the convergence of the DREAM sampling algorithm, the resulting posterior parameter distributions, and the predictive performance of the model over both the calibration and validation periods. The results are compared with those of the baseline rhyme2023 configuration to assess the net effect of the modification introduced in this work.

Two performance metrics are used throughout. The Nash-Sutcliffe Efficiency [9]:

$$NSE = 1 - \frac{\sum_{i=1}^{N}(Q_{obs,i} - Q_{sim,i})^2}{\sum_{i=1}^{N}(Q_{obs,i} - \overline{Q}_{obs})^2} \tag{6.1}$$

and the Kling-Gupta Efficiency [6]:

$$KGE = 1 - \sqrt{(r-1)^2 + (\alpha-1)^2 + (\beta-1)^2} \tag{6.2}$$

where r is the Pearson correlation coefficient, $\alpha = \sigma_{sim}/\sigma_{obs}$ is the ratio of standard deviations, and $\beta = \mu_{sim}/\mu_{obs}$ is the ratio of means. Both equal 1 for a perfect simulation. NSE weights squared residuals, making it sensitive to peak flow errors; KGE decomposes the total error into independent contributions from timing (r), variability (α), and volume bias (β), offering a more balanced diagnostic [6].

6.1 Numerical Modifications to the Baseline Model

Three structural modifications were introduced in rhyme2026 with respect to the baseline rhyme2023, in addition to the updates described in Chapter 4.

The first concerns parameter management. In the original implementation, model parameters were stored as rows of a numeric array with implicit positional indexing, making it difficult to add new parameters, assign prior distributions, or flag which entries are calibrated and which are fixed. In rhyme2026, each parameter is instead described by a dedicated entry in a structured table containing the name, physical units, bounds, and prior specification. The change eliminates a source of indexing errors and makes the calibration configuration self-documenting.

Table 6.1: Model parameters, bounds, and prior distributions used in the MCMC calibration. Parameters marked with an asterisk (*) are assigned an informative prior; all others use a uniform prior within the specified bounds. Parameters u and D_h are fixed and not included in the calibration.

Parameter	**Description**	**Units**	**Range**	**Prior**
$I_{\max}$	Maximum infiltration rate	mm/h	[5, 100]	Uniform
$n \cdot Z_r$	Effective soil storage capacity	mm	[50, 4000]	Uniform
K_0	Saturated hydraulic conductivity	mm/h	[1, 2000]	Uniform
c	Leaching non-linearity exponent	–	[1, 20]	Uniform
s_1*	Evapotranspiration threshold	–	[0.02, 1]	$\mathcal{N}(0.5, 0.05)$
α	Rapid subsurface fraction	–	[0, 1]	Uniform
β	Deep drainage fraction	–	[0, 1]	Uniform
t_{urb}	Urban reservoir residence time	h	[0.1, 40]	Uniform
t_{sup}	Surface reservoir residence time	h	[0.1, 40]	Uniform
t_{rap}	Rapid subsurface residence time	h	[0.1, 40]	Uniform
t_{prof}	Deep reservoir residence time	h	[1, 3000]	Uniform
c_d	Impervious runoff coefficient	–	[0, 1]	Uniform
α_{melt}	Degree-day melt factor	mm/d/°C	[0, 5]	Uniform
T_{melt}*	Snowmelt temperature threshold	°C	[-5, 10]	$\mathcal{N}(0, 1)$
T_{snow}*	Snowfall temperature threshold	°C	[-5, 5]	$\mathcal{N}(0, 1)$
σ	Likelihood error standard deviation	–	[0, 100]	Uniform
u (fixed)	Flow velocity	m/s	–	7.0
D_h (fixed)	Hydrodynamic dispersion coefficient	m^2/s	–	130

The second modification is the adaptive sub-stepping scheme for the soil water balance. The original forward Euler scheme advanced all fluxes simultaneously with a fixed one-hour step. The updated scheme resolves infiltration, drainage, and evapotranspiration sequentially within each hour, and refines the sub-step duration dynamically according to the condition:

$$N_s = \max\left(1, \left\lceil \frac{\Delta s_I}{0.01} \right\rceil, \left\lceil \frac{\Delta s_L}{0.01} \right\rceil\right), \qquad \delta t = \frac{\Delta t}{N_s} \tag{6.3}$$

where $\Delta s_I = I_{pot}\,\Delta t/(nZ_r)$ and $\Delta s_L = L_{pot}\,\Delta t/(nZ_r)$ are the saturation changes expected from infiltration and leaching over the full hour, evaluated at the state at the beginning of the step. The sub-step count N_s is set so that neither flux drives a saturation change exceeding 1% per sub-step. When soil moisture is near saturation or when rainfall intensity is high, N_s increases automatically, limiting the accumulation of mass balance errors that the fixed-step scheme incurs in these conditions. When the soil state is quasi-stationary, $N_s = 1$ and no computational overhead is added.

The third modification concerns geomorphological routing. In rhyme2026, the wave celerity u and hydrodynamic dispersion coefficient D_h are fixed at hydraulically derived values (Chapter 5) rather than estimated through calibration. In rhyme2023, both were free parameters with priors $u \sim \mathcal{N}(3, 0.3)$ m/s and $D_h \sim \mathcal{N}(1000, 100)$ m^2/s — prior means that differ substantially from physically-derived values of $u = 7$ m/s and $D_h = 130$ m^2/s. Fixing these two parameters reduces the dimensionality of the calibration problem from 18 to 16 free parameters.

6.2 DREAM Convergence

The DREAM algorithm was run for 2×10^5 model evaluations across 3 parallel Markov chains, initialized by Latin Hypercube Sampling (LHS) within the parameter bounds to ensure broad initial coverage of the 16-dimensional space. Convergence was monitored every 100 iterations via the Gelman-Rubin $\hat{R}$ statistic [5]. The first two thirds of each chain were discarded as burn-in, leaving approximately 22 000 posterior samples per chain (17 568 after removing rows with uninitialized values).

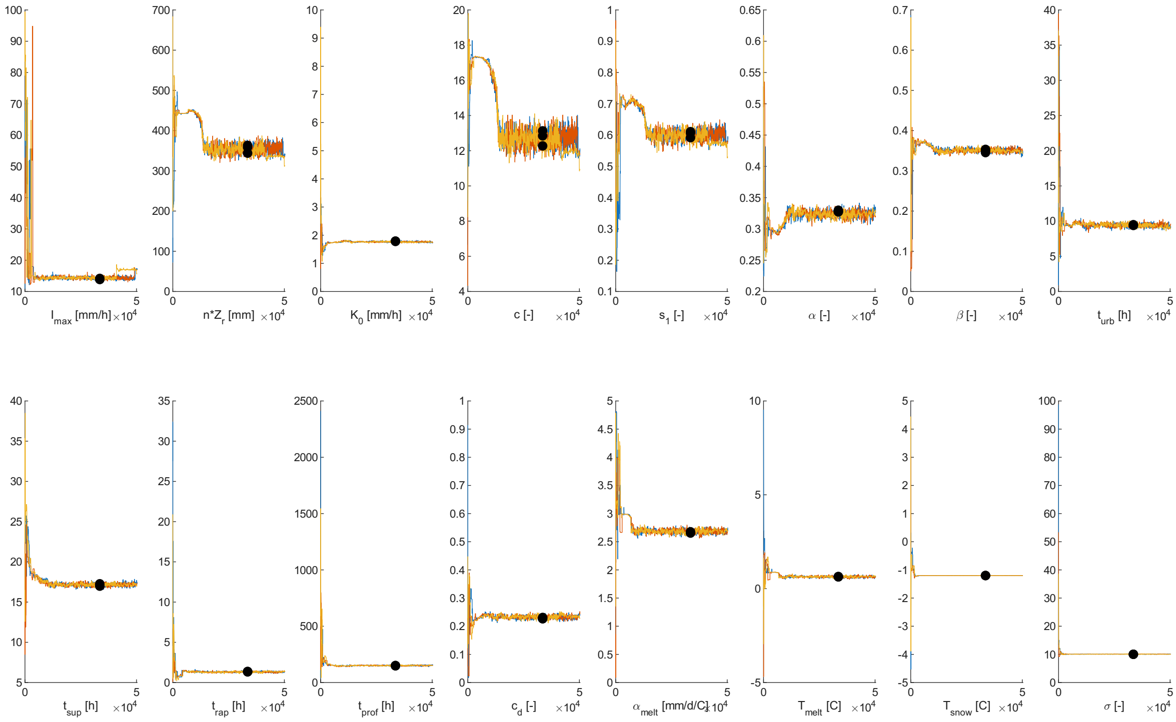

Figure 6.1: Trace plots of the three parallel Markov chains for all calibrated parameters over the DREAM run (2×10^5 model evaluations). The black dot marks the start of the posterior sample (end of the burn-in). Most parameters stabilize well before that point; $I_{\max}$ and c show the widest residual scatter, consistent with their broader posteriors.

Figure 6.1 shows the chain traces for all parameters. Most reach a stationary regime within the first 5×10^4 evaluations: K_0, s_1, α, β, t_{rap}, T_{melt}, T_{snow}, and σ all show tight chain overlap well before the burn-in cutoff. The parameters I_{max} and c exhibit slightly higher residual oscillation throughout the run — not a sign of non-convergence, but of a genuinely broader posterior reflecting weaker identifiability of these two parameters from discharge data alone.

The final $\hat{R}$ values, reported in Table 6.2, are uniformly close to 1. The maximum across all parameters is $\hat{R} = 1.0017$, well below the 1.05 threshold commonly used to declare convergence [5], and all remaining parameters round to 1.000 at three decimal places.

Table 6.2: Gelman-Rubin $\hat{R}$ statistic at the end of the DREAM run, computed over the last 33 334 samples per chain.

Parameter	$\hat{R}$
$I_{\max}$	1.0017
$n \cdot Z_r$	1.0002
K_0	1.0000
c	1.0003
s_1	1.0001
α	1.0000
β	1.0000
t_{urb}	1.0000
t_{sup}	1.0000
t_{rap}	1.0000
t_{prof}	1.0000
c_d	1.0000
α_{melt}	1.0000
T_{melt}	1.0000
T_{snow}	1.0000
σ	1.0000

6.3 Posterior Parameter Distributions

Table 6.3 reports the Maximum A Posteriori (MAP) estimate, posterior mean, and 95% credible interval for each parameter.

Most parameters are well identified: their posteriors are substantially narrower than the corresponding priors, and all MAP estimates lie within the prior bounds.

K_0 converges to 1.758 mm/h, near the lower end of its prior range $[1, 2000]$ mm/h, with a 95% credible interval of only 0.048 mm/h. The precision reflects the strong imprint that saturated conductivity leaves on recession limb shape. In combination with the nonlinearity exponent $c = 11.97$, this produces a strongly threshold-like drainage function: leaching from the root zone remains negligible at low saturation and increases sharply as the soil approaches full saturation. The implication is that surface runoff, rather than subsurface drainage, is the dominant discharge-generating mechanism for the moderate events in this catchment.

s_1 converges to a MAP of 0.578, slightly above the prior mean of 0.5 [8]. The posterior

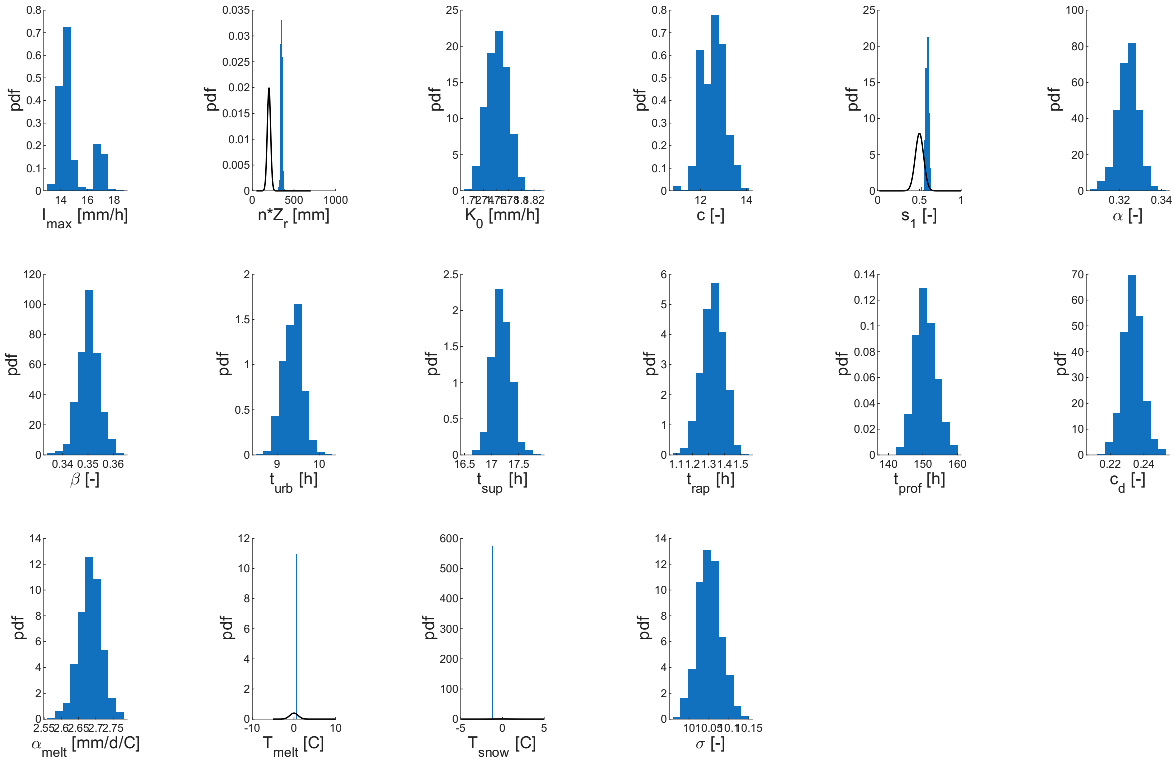

Figure 6.2: Marginal posterior distributions of the 16 calibrated parameters after DREAM burn-in. Filled histograms show the posterior sample; dashed lines show the prior (uniform or Gaussian). Informative Gaussian priors are overlaid for s_1, T_{melt}, and T_{snow}.

Table 6.3: Posterior statistics for 16 calibrated parameters of rhyme2026. MAP: Maximum A Posteriori estimate. CI: 95% credible interval. Parameters u and D_h are fixed and excluded.

Parameter	Units	MAP	Mean	$\mathrm{CI}_{2.5}$	$\mathrm{CI}_{97.5}$
I_{max}	mm/h	17.04	15.45	13.65	17.34
$n \cdot Z_r$	mm	337.73	346.53	332.28	371.84
K_0	mm/h	1.758	1.759	1.730	1.791
c	–	11.97	12.38	11.67	13.54
s_1	–	0.578	0.589	0.564	0.627
α	–	0.325	0.324	0.313	0.334
β	–	0.348	0.350	0.341	0.359
t_{urb}	h	9.236	9.293	8.874	9.871
t_{sup}	h	17.086	17.208	16.903	17.584
t_{rap}	h	1.367	1.324	1.186	1.444
t_{prof}	h	150.68	151.64	145.83	158.07
c_d	–	0.236	0.233	0.223	0.243
α_{melt}	mm/d/°C	2.711	2.686	2.630	2.737
T_{melt}	°C	0.648	0.636	0.565	0.707
T_{snow}	°C	-1.201	-1.201	-1.202	-1.200
σ	m^3/s	10.062	10.051	9.993	10.107

is narrower than the prior but comfortably within its support, indicating that the discharge record does provide information on this parameter, though not enough to dominate the prior.

The snow thresholds behave quite differently from each other. T_{snow} converges to -1.201 °C with an exceptionally tight posterior — the 95% credible interval spans only 0.002 °C, far narrower than the prior $\mathcal{N}(0, 1)$. The discharge record is apparently very informative about the rain-snow transition temperature, likely because the timing of snowpack accumulation has a large effect on the spring hydrograph. T_{melt}, by contrast, has a wider posterior (CI width ≈ 0.14 °C) and converges to 0.648 °C, close to the physical expectation for an Alpine catchment where melting begins near 0 °C.

The residence times of the four reservoirs form the expected hierarchy. $t_{rap} \approx 1.4$ h captures fast preferential flow; $t_{urb} \approx 9.2$ h represents the urban direct-runoff component; $t_{sup} \approx 17.1$ h governs surface runoff from pervious area; and $t_{prof} \approx 150.7$ h controls the slow baseflow release. All four are well constrained, with credible intervals spanning less than 20% of the MAP value in each case.

The likelihood error standard deviation σ converges to 10.06 m^3/s with a tight posterior (CI width 0.11 m^3/s), indicating that the residual noise is stable and consistent across the calibration period.

6.4 Calibration and Validation Performance

Performance metrics for both model configurations are reported in Table 6.4.

Over the calibration period, rhyme2026 achieves NSE = 0.875 and KGE = 0.817,

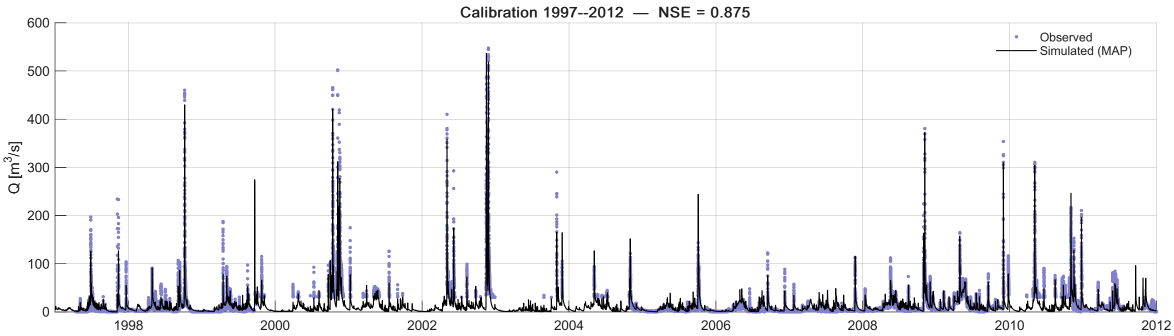

Figure 6.3: Simulated and observed discharge at the Ponte Mas over the calibration period (1997–2012). Solid line: MAP simulation. Coloured dots: observed hourly discharge retained after quality filtering.

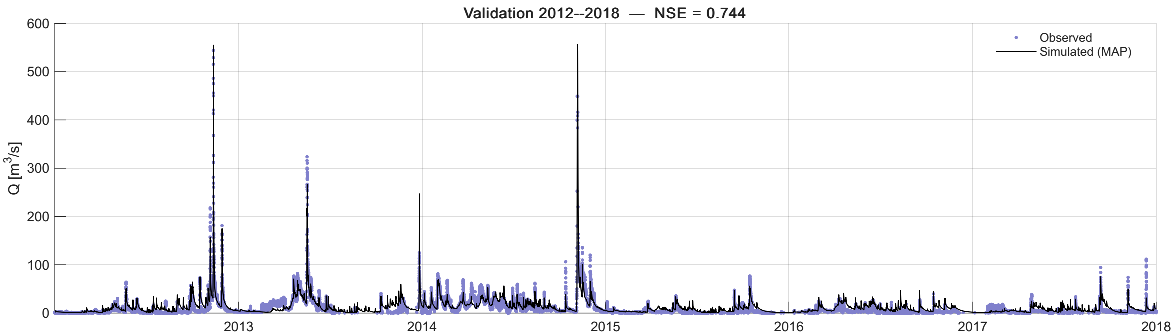

Figure 6.4: Model performance over the validation period (January 2012 – January 2018). Layout as in Figure 6.3.

reproducing the seasonal cycle, snowmelt-driven spring freshets, and the main autumn flood peaks (Figure 6.3). rhyme2023 scores somewhat higher (NSE = 0.887, KGE = 0.917). Over validation, both models degrade: rhyme2026 reaches NSE = 0.744, KGE = 0.639, against NSE = 0.796, KGE = 0.796 for the baseline (Figure 6.4).

The KGE decomposition points to the volume bias β as the primary source of the performance gap. In calibration, $\beta = 1.137$ corresponds to a 14% overestimation of mean discharge; by validation, β rises to 1.335, a 33% overestimation. The timing ($r = 0.882$) and variability ($\alpha = 0.940$) components remain satisfactory throughout, indicating that the model correctly captures the shape and phasing of discharge fluctuations but consistently generates too much runoff volume.

Figure 6.5 shows the model output over a nine-month window spanning contrasting hydrological conditions. During summer (July–August 2008), discharge is dominated by slow baseflow (Q_{prof}, black), with rapid subsurface contributions (Q_{rap}, cyan) responding to isolated precipitation events. The model tends to overestimate discharge during this low-flow period, consistent with the summer bias discussed in Section 6.5. The November 2008 flood event provides a different picture: the model reproduces the observed peak well, and the pathway decomposition shows that surface runoff (Q_{sup}, orange) dominates the peak response, consistent with the threshold-like leaching function ($K_0 = 1.76$ mm/h, $c = 11.97$) that activates sharply when the soil approaches saturation under sustained precipitation input. Rating-curve uncertainty at Ponte Mas is non-negligible at high flows, where the stage-discharge relationship must be extrapo-

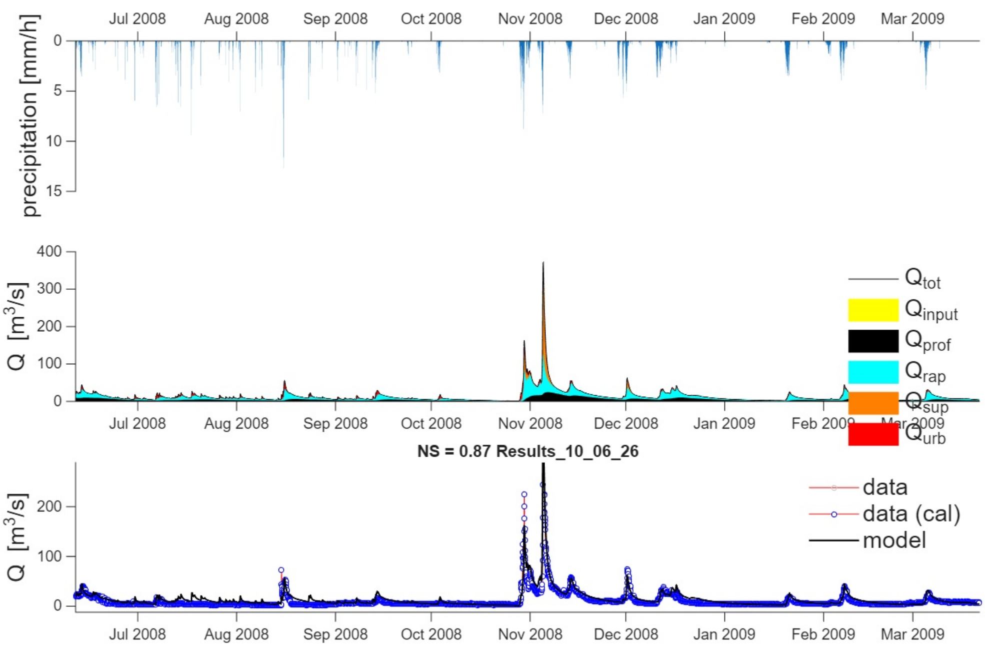

Figure 6.5: rhyme2026 simulation over the period July 2008 – March 2009, illustrating model behaviour across contrasting flow regimes. Top: hourly basin-averaged precipitation. Middle: simulated discharge decomposed by flow pathway (Q_{prof}, Q_{rap}, Q_{sup}, Q_{urb}). Bottom: MAP simulation (black) against observed discharge; quality-filtered observations used in calibration are shown in blue.

lated beyond the range of direct velocity measurements; the calibrated error standard deviation $\sigma = 10.06$ m^3/s absorbs both model error and measurement uncertainty indistinguishably.

The water balance comparison in Figure 6.6 gives a more direct reading of the structural difference between the two configurations. In rhyme2026, the four components — discharge (38%), actual ET (37%), deep recharge (25%), and storage change (<1%) — are consistent with the expected water balance of a forested Alpine catchment receiving 1352 mm of mean annual precipitation, with an implied mean annual ET roughly 500 mm. In rhyme2023, ET absorbs 60% of total precipitation (≈810 mm/year), leaving only 6% as deep recharge. In that configuration, evapotranspiration was scaled by a single free calibration parameter — effectively a spatially uniform, time-constant crop coefficient — with no land-cover constraint. The calibrated value of this parameter implies a basin-averaged $K_c \approx 1.8$, which is physically unrealistic: even the most actively transpiring CLC classes present in the basin are assigned mid-season K_c values of 1.0–1.3 in the [10] table (Table 4.2), and basin-averaged values exceeding 1.3 would require canopy interception and bare-soil evaporation to systematically exceed reference ET_0.

The DREAM calibration drove K_c toward that unrealistic value because doing so reduced the discharge bias penalized by the likelihood function. In effect, evapotranspiration served as a global correction term: rather than improving the representation of individual processes, the algorithm removed excess water from the simulated hydrograph by routing it through the ET pathway. The better scalar metrics of rhyme2023

Table 6.4: Performance metrics for rhyme2023 and rhyme2026 over the calibration (1997–2012) and validation (2012–2018) periods. KGE is decomposed into Pearson correlation r, variability ratio α, and volume bias β.

Model	**Period**	**NSE**	**KGE**	r	α	β
rhyme2023	Calibration	0.887	0.917	0.942	0.941	1.004
rhyme2026	Calibration	0.875	0.817	0.938	0.895	1.137
rhyme2023	Validation	0.796	0.796	0.905	1.023	1.179
rhyme2026	Validation	0.744	0.639	0.882	0.940	1.335

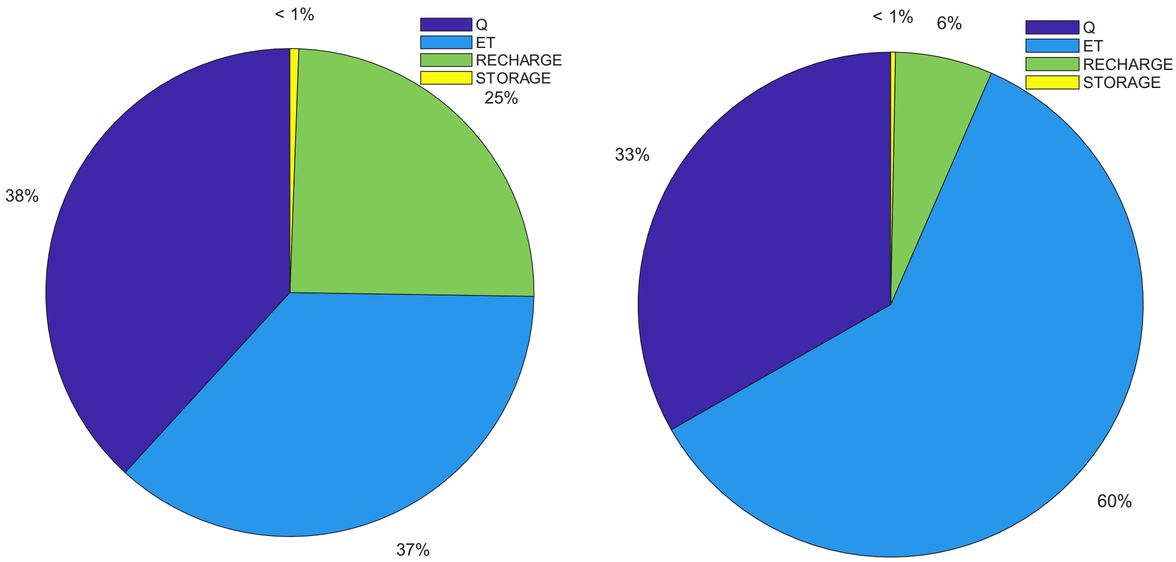

(a) rhyme2026 (b) rhyme2023

Figure 6.6: Mean annual water balance partitioning for rhyme2026 and rhyme2023 over the 1996–2019 simulation period, expressed as fractions of total precipitation. Q: discharge; ET: actual evapotranspiration; RECHARGE: deep percolation; STORAGE: net change in soil and snow storage. The 60% ET fraction in rhyme2023 implies a basin-averaged $K_c \approx 1.8$, which is incompatible with the land cover composition of the basin.

are partly an artefact of this mechanism. The superior performance in validation — where rhyme2023 maintains NSE = 0.796 against rhyme2026's 0.744 — suggests that the compensation generalizes across time, but it does so by exploiting a degree of freedom that has no physical basis. In rhyme2026, fixing u, D_h, and K_c to physically derived or land-cover-constrained values removes these compensation channels, exposing the residual structural limitations of the model. The performance gap between the two versions should be read in that light.

6.5 Seasonal Bias Analysis

To characterize the temporal structure of the volumetric overestimation, the monthly volume bias $\beta_m = \mu_{\text{sim,m}}/\mu_{\text{obs,m}}$ was computed over the validation period for each calendar month. Results are reported in Table 6.5 and Figure 6.7.

The bias pattern has a clear seasonal structure. February and March show underestimation ($\beta = 0.79$ and $\beta = 0.87$ respectively), while from June onward the model

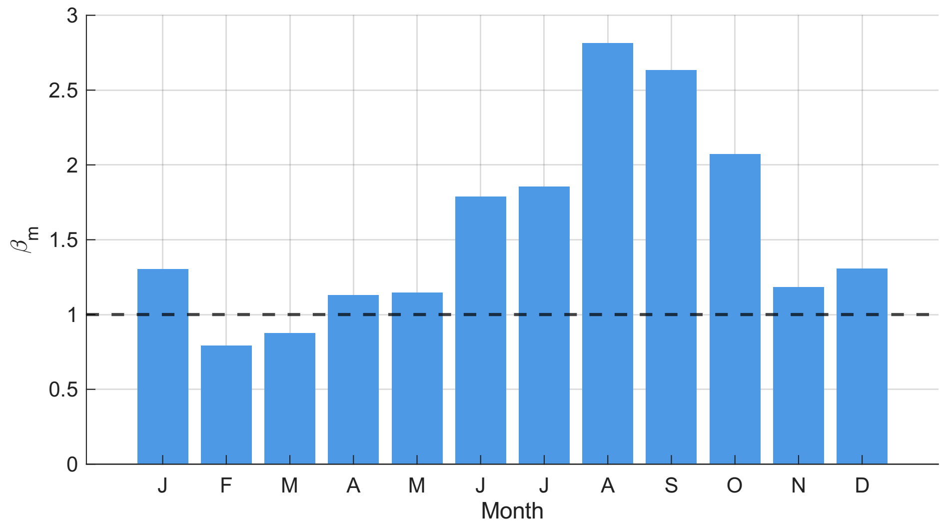

Figure 6.7: Monthly volume bias β_m of rhyme2026 over the validation period (2012–2018). The dashed line at $\beta_m = 1$ marks unbiased simulation.

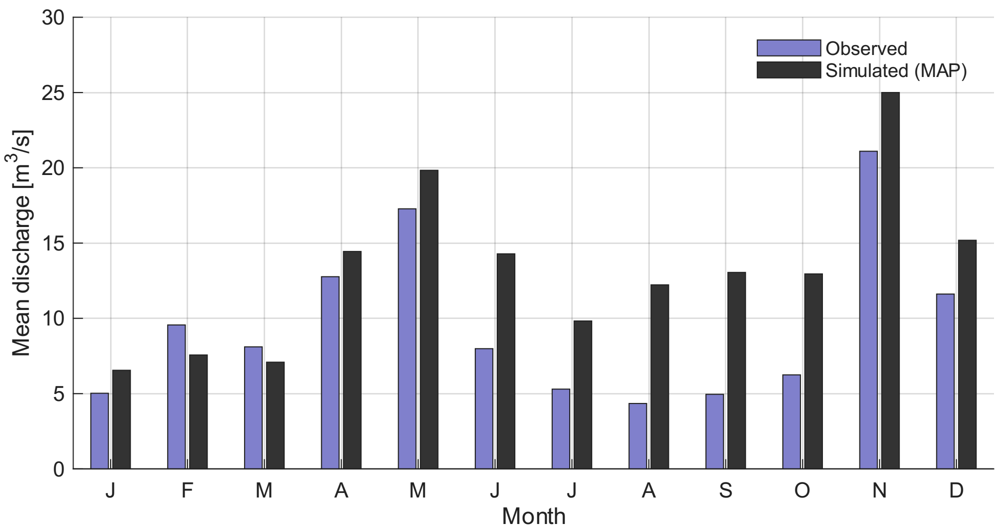

Figure 6.8: Mean monthly observed and simulated discharge at Ponte Mas over the validation period (2012–2018). The absolute overestimation in summer is substantial despite the low flow magnitudes; August and September show the largest absolute errors of the year (Table 6.6).

Table 6.5: Monthly volume bias β_m of rhyme2026 over the validation period (2012–2018). Values above 1 indicate overestimation; values below 1 indicate underestimation.

	Jan	Feb	Mar	Apr	May	Jun	Jul	Aug	Sep	Oct	Nov	Dec
β_m	1.30	0.79	0.87	1.13	1.15	1.79	1.85	2.81	2.63	2.07	1.18	1.31

Table 6.6: Mean monthly observed and simulated discharge at Ponte Mas over the validation period (2012–2018), with absolute and relative error.

Month	Q_{obs} **[m^3/s]**	Q_{sim} **[m^3/s]**	**Abs. error [m^3/s]**	**Rel. error [%]**
Jan	5.02	6.55	1.53	30.4
Feb	9.56	7.57	−1.99	−20.8
Mar	8.11	7.09	−1.02	−12.6
Apr	12.77	14.44	1.68	13.1
May	17.28	19.83	2.56	14.8
Jun	7.99	14.28	6.30	78.9
Jul	5.30	9.83	4.53	85.4
Aug	4.34	12.23	7.88	181.4
Sep	4.95	13.05	8.10	163.5
Oct	6.25	12.95	6.71	107.4
Nov	21.10	25.00	3.90	18.5
Dec	11.61	15.19	3.57	30.8

systematically overestimates, with the ratio peaking in August ($\beta = 2.81$) and September ($\beta = 2.63$) before returning toward neutral in November. The transition months of May and November are near-unbiased ($\beta = 1.15$ and $\beta = 1.18$), suggesting that the errors are concentrated at the seasonal extremes rather than distributed uniformly across the year.

Before interpreting the monthly ratios, the absolute error context matters. The observed mean discharge in August is only 4.34 m^3/s, confirming that this is the low-flow season; yet the model generates 12.23 m^3/s, an absolute overestimation of 7.88 m^3/s. September shows the largest absolute error of the year at 8.10 m^3/s. These are not negligible in terms of the low-flow water balance, though their contribution to the overall NSE remains limited because individual flood peaks — where residuals can reach several tens of m^3/s — dominate the squared-error metric. The summer errors therefore represent a structural deficiency in the low-flow regime that is largely invisible in the scalar performance metrics.

The winter underestimation in February–March coincides with the period of maximum snowpack and the onset of spring melt. The degree-day module may delay the transition from accumulation to melt relative to the actual catchment response, generating insufficient liquid water input to the soil in early spring. The tightly calibrated melt threshold $T_{\text{melt}} = 0.648$ °C is unlikely to be the sole cause — the posterior is narrow, meaning the calibration had little room to adjust this parameter — so the limitation may instead reflect the spatial averaging of temperature inputs across sub-catchments spanning a wide elevation range.

The summer and autumn overestimation is more directly attributable to evapotranspiration. With $s_1 = 0.578$, water stress begins to reduce actual ET once the soil drops below 57.8% of capacity. If the soil regularly falls below this threshold during dry summer months, actual ET falls below $ET_c = K_c \cdot ET_0$, and the unremoved water eventually drains as baseflow. The K_c values from [10] for the classes of the basin may also be underestimates for the northeastern Alpine environment: coniferous forests at high elevation can sustain substantial transpiration through prolonged dry periods, a behavior that generic continental K_c tables may not fully capture. An additional mechanism not represented in the current model structure is groundwater–river exchange: in Alpine catchments, bank storage and hyporheic flux can remove water from the active runoff system during low flows through pathways that bypass the model's reservoir scheme entirely, effectively reducing simulated baseflow relative to observed. These processes are inherently more relevant in summer, when event-driven fluxes are small and the low-flow regime dominates.

Chapter 7

Conclusions

The central objective of this thesis was to update and calibrate the RHYME hydrological model for the Cordevole basin at Ponte Mas, addressing three specific limitations of the baseline rhyme2023 configuration: a spatially uniform, non-seasonal crop coefficient; a fixed-step explicit scheme for the soil water balance; and geomorphological routing parameters estimated through hydrological calibration rather than hydraulic analysis.

Four modifications were implemented in rhyme2026. The crop coefficient was replaced by a monthly, sub-catchment specific field derived from the CORINE Land Cover dataset via matrix multiplication with the seasonal coefficients of [10]. Reference evapotranspiration was computed using the FAO-56 Penman-Monteith equation, replacing a simplified temperature-driven routine that was shown to overestimate ET_0 systematically by approximately 0.056 mm/day relative to the Penman-Monteith reference. An adaptive sub-stepping scheme was introduced for the soil water balance, resolving infiltration, drainage, and evapotranspiration sequentially and refining the sub-step duration when the expected saturation change within a single hour exceeds 1%, reducing mass balance errors during high-intensity events. Finally, the wave celerity u and dispersion coefficient D_h were fixed to hydraulically derived values from a dedicated HEC-RAS simulation of the September 1999 flood: $u = 7$ m/s from the observed peak-to-peak travel time, and $D_h = 130$ m^2/s, a value for which the RMSE surface is essentially flat (RMSE difference from the formal grid-search optimum: 0.007 m^3/s) due to the dominance of advection over dispersion at the reach scale (Péclet number $Pe \approx 994$).

The DREAM calibration over the 1997–2012 showed good converging properties, with a maximum Gelman-Rubin statistic of $\hat{R} = 1.0017$ across all 16 free parameters and 17 568 valid posterior samples. The posterior distributions are physically interpretable. The combination of low $K_0 = 1.76$ mm/h and high nonlinearity exponent $c = 11.97$ produces a strongly threshold-like drainage function, implying that surface runoff — rather than subsurface flow — is the dominant discharge-generating mechanism for moderate events. $T_{snow} = -1.201$ °C is constrained to within 0.002 °C, indicating that the rain-snow partitioning threshold is tightly identified from the discharge record. The four reservoir residence times form the expected timescale hierarchy from fast preferential flow ($t_{rap} \approx 1.4$ h) to slow baseflow ($t_{prof} \approx 150.7$ h).

Predictive performance is adequate but lower than rhyme2023. rhyme2026 achieves NSE = 0.875 and KGE = 0.817 in calibration and NSE = 0.744, KGE = 0.639 in validation, against NSE = 0.887/KGE = 0.917 and NSE = 0.796/KGE = 0.796 for the baseline. The primary driver of the gap is the volume bias β, which reaches 1.335 in validation. The seasonal bias analysis shows that the overestimation is concentrated in summer and early autumn (β peaking at 2.81 in August), while the model underestimates discharge in February–March, likely due to delayed snowmelt onset. The summer bias corresponds to absolute overestimations of 7.88 m^3/s in August and 8.10 m^3/s in September (Table 6.6), which are among the largest monthly absolute errors of the year despite occurring in the low-flow season. Their contribution to the overall NSE remains limited because individual flood peaks dominate the squared-error metric. These errors may partly reflect the absence of groundwater–river exchange processes, which can remove water from the active runoff system through hyporheic pathways not represented in the current model structure.

The water balance comparison with rhyme2023 (Figure 6.6) clarifies why the baseline performs better despite its simpler evapotranspiration formulation. In rhyme2023, the free crop coefficient was driven by calibration to a basin-averaged value of approximately 1.8, implying mean annual ET of roughly 810 mm — physically incompatible with any of the CLC classes present in the basin. This artificially high ET compensated for a positive discharge bias through the evapotranspiration pathway rather than through improved process representation. Fixing K_c to land-cover-derived values in rhyme2026 removes this degree of freedom, and the resulting performance gap is better understood as an exposure of structural limitations that were previously hidden, not as a deterioration of model quality.

The meteorological trends analysis over 1996–2019 shows a statistically significant increase in wind speed across all four seasons ($p < 0.01$), making it the dominant driver of the long-term positive ET_0 trend. Temperature warming is significant in summer and autumn only. This reinforces the choice of the FAO-56 Penman-Monteith formulation: unlike the temperature-based routine of rhyme2023, it explicitly represents the aerodynamic term, which carries the strongest and most consistent long-term signal in the forcing record.

Several avenues remain open for further development. On the evapotranspiration side, replacing the Nistor K_c table with remote-sensing-based vegetation indices calibrated for the northeastern Alpine environment would provide a more locally representative seasonal signal and likely reduce the summer overestimation. On the snow side, the degree-day module could be extended to account for elevation-dependent melt rates or wind-driven redistribution, which may explain part of the February–March underestimation. From a calibration standpoint, replacing the homoscedastic Gaussian likelihood with a heteroscedastic formulation — weighting residuals by observed discharge — would place more emphasis on peak flow reproduction and reduce the tendency to minimize average error at the cost of extreme events. Operationally, extending rhyme2026 to the full Piave network within the IMAGeOnFEWS platform would allow the contributions of this work to be evaluated at the catchment scale for which the forecasting system was designed.

Bibliography

[1] Richard G Allen, Luis S Pereira, Dirk Raes, Martin Smith, et al. Fao irrigation and drainage paper no. 56. *Rome: food and agriculture organization of the United Nations*, 56(97):e156, 1998.

[2] Gary W Brunner. Hec-ras river analysis system. hydraulic reference manual. version 1.0. 1995.

[3] Copernicus Land Monitoring Service. Copernicus land monitoring service. *European Environment Agency (EEA)*, 2018.

[4] Elena Crestani, Giulia Passadore, Daniele Pietro Viero, Luca Carniello, Enrico Bertuzzo, Bruno Matticchio, Luigi D'Alpaos, Andrea Rinaldo, et al. Sistema integrato di previsione delle piene in tempo reale nel bacino idrografico del piave. In *Atti del XXXVIII Convegno Nazionale di Idraulica e Costruzioni Idrauliche*. 2022.

[5] Andrew Gelman and Donald B Rubin. Inference from iterative simulation using multiple sequences. *Statistical science*, 7(4):457–472, 1992.

[6] Hoshin V Gupta, Harald Kling, Koray K Yilmaz, and Guillermo F Martinez. Decomposition of the mean squared error and nse performance criteria: Implications for improving hydrological modelling. *Journal of hydrology*, 377(1-2):80–91, 2009.

[7] Regine Hock. Temperature index melt modelling in mountain areas. *Journal of hydrology*, 282(1-4):104–115, 2003.

[8] Francesco Laio, Amilcare Porporato, Luca Ridolfi, and Ignacio Rodriguez-Iturbe. Plants in water-controlled ecosystems: active role in hydrologic processes and response to water stress: Ii. probabilistic soil moisture dynamics. *Advances in water resources*, 24(7):707–723, 2001.

[9] J.E. Nash and J.V. Sutcliffe. River flow forecasting through conceptual models part i — a discussion of principles. *Journal of Hydrology*, 10(3):282–290, 1970.

[10] Mărgărit-Mircea Nistor. Projection of annual crop coefficients in italy based on climate models and land cover data. *Geographia Technica*, 13(2), 2018.

[11] Lorenzo Picco, Luca Mao, Emanuel Rigon, Johnny Moretto, Diego Ravazzolo, Fabio Delai, Mario Aristide Lenzi, et al. An update of the sediment fluxes investigation in the rio cordon (italy) after 25 years of monitoring. *Journal of Agricultural Engineering*, 43(3):e17–e17, 2012.

[12] Andrea Rinaldo and IGNACIO RODRIGUEZ-ITURBE. Geomorphological theory of the hydrological response. *Hydrological processes*, 10(6):803–829, 1996.

[13] Bettina Schaefli, Ludovico Nicótina, Cedric Imfeld, P Da Ronco, Enrico Bertuzzo, and A Rinaldo. Sehr-echo v1. 0: a spatially explicit hydrologic response model for ecohydrologic applications. *Geoscientific Model Development*, 7(6):2733–2746, 2014.

[14] Jasper A Vrugt, James M Hyman, Bruce A Robinson, Dave Higdon, and Cees GH Diks. Accelerating markov chain monte carlo simulation by differential evolution with self-adaptive randomized subspace sampling. Technical report, Los Alamos National Laboratory (LANL), 2007.